AGU PUBLICATIONS

Journal of Advances in Modeling Earth Systems

RESEARCH ARTICLE
10.1002/2016MS000700

Assessment of the simulation of Indian Ocean Dipole in the CESM—Impacts of atmospheric physics and model resolution

Zhixiong Yao[1,2], Youmin Tang[3,2], Dake Chen[2], Lei Zhou[2], Xiaojing Li[2], Tao Lian[2], and Siraj Ul Islam[3]

[1]College of Ocean and Earth Sciences, Xiamen University, Xiamen, China, [2]State Key Laboratory of Satellite Ocean Environment Dynamics, Second Institute of Oceanography, Hangzhou, China, [3]Environmental Science and Engineering, University of Northern British Columbia, Prince George, British Columbia, Canada

Key Points:
- We comprehensively examine the possible impacts of coupling processes on simulations of the Indian Ocean Dipole
- The IOD intensity is attributable to wind-thermocline depth feedback and thermocline depth-subsurface temperature feedback
- We analyze the relationships of IOD-monsoon, ENSO-monsoon, and IOD-ENSO

Correspondence to:
Y. Tang,
ytang@unbc.ca

Citation:
Yao, Z., Y. Tang, D. Chen, L. Zhou, X. Li, T. Lian, and S. Ul Islam (2016), Assessment of the simulation of Indian Ocean Dipole in the CESM—Impacts of atmospheric physics and model resolution, *J. Adv. Model. Earth Syst.*, *8*, 1932–1952, doi:10.1002/2016MS000700.

Received 28 APR 2016
Accepted 15 NOV 2016
Accepted article online 18 NOV 2016
Published online 22 DEC 2016

Abstract This study examines the possible impacts of coupling processes on simulations of the Indian Ocean Dipole (IOD). Emphasis is placed on the atmospheric model resolution and physics. Five experiments were conducted for this purpose, including one control run of the ocean-only model, four coupled experiments using two different versions of the Community Atmosphere Model (CAM4 and CAM5) and two different resolutions. The results show that the control run could effectively simulate various features of the IOD. The coupled experiments run at the higher resolution yielded more realistic IOD period and intensity than their counterparts at the low resolution. The coupled experiments using CAM5 generally showed a better simulation skill in the tropical Indian SST climatology and phase-locking than those using CAM4, but the wind anomalies were stronger and the IOD period were longer in the former experiments than in the latter. In all coupled experiments, the IOD intensity was much stronger than the observed intensity, which is attributable to wind-thermocline depth feedback and thermocline depth-subsurface temperature feedback. The CAM5 physics seems beneficial for the simulation of summer rainfall over the eastern equatorial Indian Ocean and the CAM4 physics tends to produce less biases over the western equatorial Indian Ocean, whereas the higher resolution tends to generate unrealistically strong meridional winds. The IOD-ENSO relationship was captured reasonably well in coupled experiments, with improvements in CAM5 relative to CAM4. However, the teleconnection of the IOD-Indian summer monsoon and ENSO-Indian summer monsoon was not realistically simulated in all experiments.

1. Introduction

The Indian Ocean Dipole (IOD) mode, identified by *Saji et al.* [1999] and *Webster et al.* [1999], is the most significant interannual variability in the tropical Indian Ocean. A positive phase of IOD is characterized by positive sea surface temperature anomalies (SSTAs) in the west tropical Indian Ocean and negative SSTA in the southeast, whereas the opposite is true for a negative IOD phase. The IOD has a broadband period of 2–5 year [*Huang and Kinter*, 2002] and exerts a significant impact on both atmospheric and oceanic circulation anomalies, such as anomalies in African rainfall, Indian summer monsoon rainfall, Australian rainfall, and the Indonesian throughflow as well as SSTAs in the western-central equatorial Pacific [*Annamalai et al.*, 2003; *Ashok et al.*, 2003; *Vinayachandran et al.*, 2009; *Lian et al.*, 2014; *Li, J. et al.*, 2016].

Intensive research has been dedicated to simulating climate variabilities of interest using coupled models, which is a necessary step toward understanding and predicting such climate variabilities. Usually, for a given prediction target, a widely used strategy in the prediction community is to first improve the performance of relevant simulations to realistically reproduce its major characteristics. A typical example is the El Niño-Southern Oscillation (ENSO), an interannual variability over the tropical Pacific Ocean, which is the phenomenon for which the best prediction skill at seasonal time scales is currently available.

Considerable studies have been conducted on the simulation of the IOD. For example, *Vinayachandran et al.* [2002] examined the evolution of the IOD using an ocean model driven by the National Centers for Environmental Prediction (NCEP) fluxes for the period of 1975–1998 and found that the model dipole mode index (DMI) agreed well with the corresponding observations. Using the Hadley Centre coupled models, *Spencer et al.* [2005] conducted coupled model experiments and found that the simulation was improved substantially by increasing the resolution of the ocean model. *Cai et al.* [2005] reproduced several realistic features of the IOD, including the strong seasonal phase-locking, in the Commonwealth Scientific and Industrial Research Organization (CSIRO) Mark 3 climate model. However, some concerns still exist regarding the modeling of the

IOD using a coupled model. For example, the dipoles do not terminate completely but instead persist through the following year [*Iizuka et al*., 2000; *Spencer et al*., 2005]. In particular, the IOD intensity in almost all models is stronger than the observed intensity [*Liu et al*., 2011; *Cai and Cowan*, 2013; *Liu et al*., 2014]. Thus, it is interesting to investigate in detail several possible impacts of model configurations relevant to the inherent physical and dynamical processes on IOD simulations, especially on the IOD intensity.

Among the models that are widely used in the climate modeling community, the National Center for Atmospheric Research (NCAR) Community Earth System Model (CESM) and various versions of its predecessor, the Community Climate System Model (CCSM), have long played an important role. This model was created by NCAR in 1983 as a freely available global atmosphere model for use by the broad climate research community and began to be developed into a fully coupled atmosphere-ocean-land-sea ice model in 1994. Now, the CESM has become one of most popular climate models in the world and is widely used for various studies of climate variability, climate prediction, and climate change [e.g., *Hurrell et al*., 2013].

In this work, we investigate the simulation of the IOD using the CESM, including the IOD features that can and cannot be well captured by the model. Compared with the simulations of certain other climate variabilities including MJO [*Subramanian et al*., 2011; *Cai et al*., 2013], the ENSO [*Neale et al*., 2008; *Deser et al*., 2012], and the Atlantic meridional overturning circulation (MOC) [*Danabasoglu*, 2008; *Renold et al*., 2010], few simulations of the IOD using the CESM have recently been reported in the literature. *Li et al*. [2002] analyzed the atmosphere-ocean feedback process during the development of the IOD in a standalone NCAR ocean model, not a coupled model. Thus, this work offers a good complement to the previous work of the CESM community, which should be interesting and beneficial for the further development of the CESM. More importantly, this work emphasizes possible physical processes that may impact the simulation of major features of the IOD, including the horizontal resolution and atmospheric physics of the model. To this end, we conduct five experiments with different resolutions and atmospheric physics in the CESM to examine and diagnose its efficacy for IOD simulations.

Many studies have addressed the impacts of model resolution and atmospheric physics on the simulation of various atmospheric and oceanic variables in the CCSM and CESM. For example, *Gent et al*. [2010] found significant improvements in SST simulations in major upwelling regions and in the precipitation patterns of the summer Asian monsoon when the atmosphere resolution was increased from 2° to 0.5°. *Kirtman et al*. [2012] reported that an increased oceanic resolution leads to better SST gradients in the North Atlantic. *Islum et al*. [2013] and *Li, X. et al*. [2016] found that the changes to the parameterization scheme in the Community Atmosphere Model version 5 (CAM5) are beneficial for simulating the mean Asian monsoon climatology and the features of the MJO, respectively. However, these studies did not focus on the IOD. Thus, it is of considerable interest to also explore the impacts of these processes on the IOD.

The remainder of this paper is structured as follows. Section 2 briefly introduces the model configurations, the experimental design, and the observation data used in this study. The results of control and sensitive experiments using the CESM are presented in sections 3 and 4, respectively. An analysis of the Bjerknes feedback is described in section 5. A simulation of the Indian summer monsoon is presented in section 6, and a summary and discussion follow in section 7.

2. Model, Experiment, and Observational Data

The model used in this study is the latest version (1.2) of the CESM, which was released in December 2013 and consists of several individual components that simultaneously simulate the Earth's atmosphere, ocean, land, land-ice, and sea-ice and are connected by a coupler [*Vertenstein et al*., 2013]. Descriptions and evaluations of the model components are included in CCSM4, which is a previous version of the CESM [*Gent et al*., 2011]. Compared to CCSM4, the most important improvement in the CESM is the newest version of the CAM component, CAM5. The century-scale transient climate response, global mean, and spatial patterns of cloud radiative forcing in CAM5 are more realistic than those in previous CAM versions, although several significant shortcomings remain to be addressed [*Kay et al*., 2012; *Hurrell et al*., 2013].

Parallel Ocean Program version 2 (POP2) [*Smith et al*., 2010] is the oceanic component of the CESM, which solves the 3-D primitive equations for ocean dynamics using the hydrostatic and Boussinesq approximations. The version used here has a nominal resolution of 1° and 60 levels in the vertical direction. Displaced-pole ocean grids are included in the POP2 release.

Table 1. Summary of the Experimental Setups, Where *N* is the Number of Levels[a]

		Ocean		Atmosphere		
Experiment Name	Atmosphere Physic	Horizontal	*N*	Horizontal	*N*	Time Period
POP2		gx1v6	60			1948–2009
CPL4(2°)	CAM4	gx1v6	60	1.9° × 2.5°	26	50 years
CPL5(2°)	CAM5	gx1v6	60	1.9° × 2.5°	30	50 years
CPL4(1°)	CAM4	gx1v6	60	0.9° × 1.25°	26	50 years
CPL5(1°)	CAM5	gx1v6	60	0.9° × 1.25°	30	50 years

[a]The forcing data were the CORE data set for the POP2 experiment and present-day climatology forcing for the CPL experiments. All CPL experiments were run for the present state of the climate and were run for 200 years from the built-in initial conditions. The results for the last 50 years were then investigated.

CAM4 [*Neale et al*., 2010] was developed by modifying several features of CAM3 [*Collins et al*., 2006], namely, the parameterization schemes for deep convection [*Neale et al*., 2008], polar filtering [*Anderson et al*., 2009], and the polar cloud fraction under extreme cold conditions [*Vavrus and Waliser*, 2008]. It uses an updated convection parameterization scheme [*Neale et al*., 2008; *Richter and Rasch*, 2008]. This model can be run using three different dynamic schemes (an Eulerian spectral scheme, a semi-Lagrangian scheme and a finite volume scheme) along with different resolution settings.

CAM5 [*Neale et al*., 2012] possesses significant modifications compared with CAM4, with a range of improvements to its representation of physical processes. It includes a new shallow convection scheme [*Park and Bretherton*, 2009], a stratiform cloud microphysical scheme [*Morrison and Gettelman*, 2008], an updated radiation scheme [*Iacono et al*., 2008], and a three-mode modal aerosol scheme (MAM3) [*Liu et al*., 2012]. The default number of vertical levels in CAM4 is 26, whereas it is 30 in CAM5.

Two different types of experiments are conducted in this study to investigate the simulation of the IOD. The first was a control experiment, in which the POP2 ocean model was forced by a prescribed (observed) forcing to produce realistic IOD variations. Second, fully coupled (CESM) experiments were conducted, from which the main features of the IOD were extracted and compared with observations. Experiments investigating the sensitivity of the IOD to the model resolution and the atmospheric physics were conducted only for the experiments of the second type, which are summarized in Table 1.

In the control run, POP2 was forced by the interannual forcing (IAF) from Version 2 of the Coordinated Ocean-ice Reference Experiments (CORE-II) data sets, which are proposed by the Climate Variability and Predictability (CLIVAR) Working Group on Ocean Model Development. The interannual forcing data considered in this study span 62 years, from 1948 to 2009; they were developed by *Large and Yeager* [2004, 2009] and were first used in *Griffies et al*. [2009]. Since that time, the CORE-II data sets have been widely applied in oceanic and climate modeling [e.g., *Sidorenko et al*., 2011]. This experiment is referred to as POP2 in Table 1.

To investigate the simulation of the IOD using the fully coupled CESM, two different CAM versions (CAM4 and CAM5) and two different horizontal resolutions were combined to generate four coupled experiments, as shown in Table 1. The lower resolution was 1.9° × 2.5° and the higher resolution was 0.9° × 1.25°. Hereafter, CPL4(2°) and CPL4(1°) denote the coupled experiments (CPL experiments) performed using CAM4 at the low and high resolutions, and CPL5(2°) and CPL5(1°) denote the coupled runs using CAM5 at the low and high resolutions. In all coupled experiments, the resolution for the ocean component was set by using a 1° × 1° Greenland Pole grid. All experiments were integrated for 100 years and were run for the present climate state, not a pre-industrial climate state. The outputs for the last 50 years are considered in the following analyses and discussions. Before running these experiments, we freely ran the coupled models for 100 years from the CESM's provided built-in initial conditions and produced a restart file corresponding to the end of the 100 year run. All experiments discussed in this study were initialized from that restart file. Thus, the 100 year coupling runs performed in this study can be viewed as equivalent to 200 year coupling runs from the built-in initial conditions. Therefore, considering that the CESM's built-in initial conditions were probably generated after training the model over a couple of years, we believe that the last 50 years of each run, which are actually equivalent to free runs of more than 200 years, can yield robust results. We also calculated the global volume-averaged kinetic energy of the upper 200 m of the ocean and found that its time evolution is very stable and exhibits no climate drift over the last 50 years (not shown).

The simulations were validated against the following data: (1) wind components from the National Centers for Environmental Prediction (NCEP) reanalysis [*Kalnay et al.*, 1996] for 1948–2009 on a 2.5°×2.5° grid, (2) SSTs from the Hadley Centre Sea Ice and Sea Surface Temperature (HadISST) data set [*Rayner et al.*, 2003] for 1948–2009 on a 1° × 1° grid, (3) 45 year European Centre for Medium-Range Weather Forecasts Re-Analysis (ERA-40) products [*Uppala et al.*, 2005], (4) Ocean temperature from the Simple Ocean Data Assimilation (SODA) data set [*Carton and Giese*, 2008] for 1948–2009 on a 0.5° × 0.5° grid, and (5) precipitation data from the Climate Prediction Center Merged Analysis of Precipitation (CMAP) [*Xie and Arkin*, 1997] for 1979–2009 on a 2.5° × 2.5° grid.

3. Simulation of the IOD in POP2

To characterize the interannual variability of the IOD, an EOF (empirical orthogonal functions) analysis was performed on the monthly SSTAs. Figures 1a and 1b show the two leading modes of the observed SSTAs over the tropical Indian Ocean, which are strongly consistent with the results of previous works [*Deser et al.*, 2010]. EOF1 explains 35% of the total variance and corresponds to a uniform variation of the SSTAs over the entire domain, i.e., the Indian Ocean Basin-wide mode (IOB). EOF2 explains 11% of the total variance and captures the IOD mode. It has been argued that the IOB mode is closely connected to the ENSO [*Klein et al.*, 1999; *Venzke et al.*, 2000], but it is not clear whether the IOD intrinsically co-occurs with the ENSO [*Baquero-Bernal et al.*, 2002; *Yu and Lau*, 2005] or is an independent variability over the Indian Ocean [*Saji et al.*, 1999; *Iizuka et al.*, 2000].

The first two leading EOF modes of the POP2 SSTAs are shown in Figures 1c and 1d. The POP2 EOF1 is comparable to its observed counterpart, except for some differences off the Sumatra-Java coast. The modeled

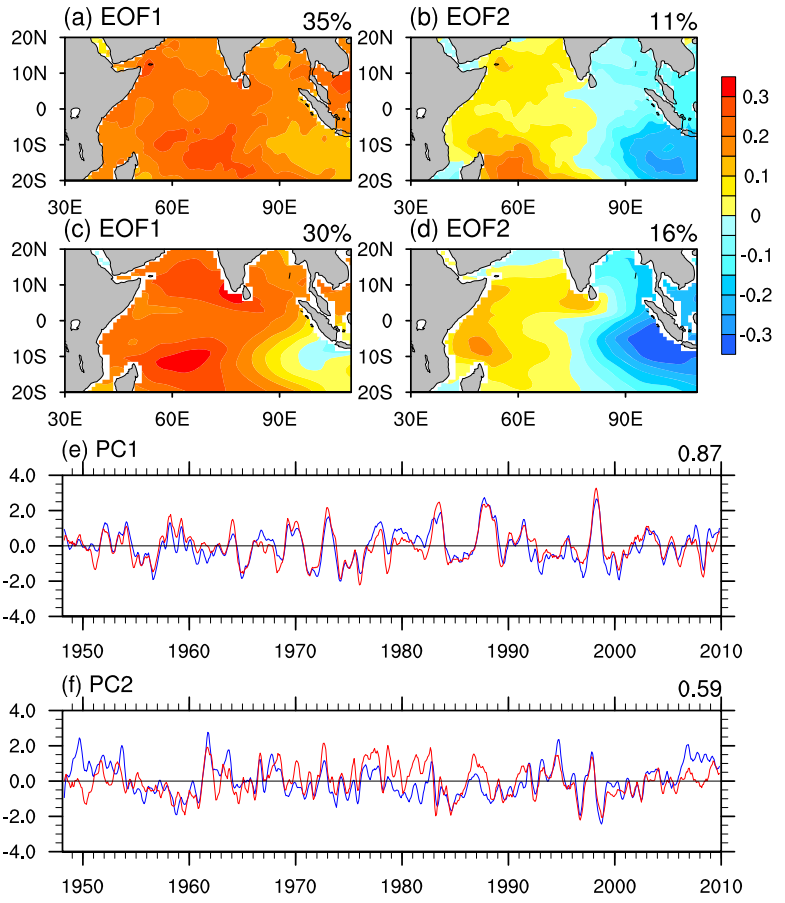

Figure 1. (a and b) The two leading EOFs for the sea surface temperature anomalies derived from the HadISST data set and (c and d) from POP2. The proportions indicated at the top right of plots (a–d) represent the variance contributions for each EOF mode. (e) The first and (f) second principal components (PCs) correspond to these EOFs from the HadISST data set (red) and POP2 (blue). Both time series are normalized with respect to their standard deviations. The proportions indicated at the top right of plot (e and f) represent the correlations of the PCs between the HadISST and POP2 results.

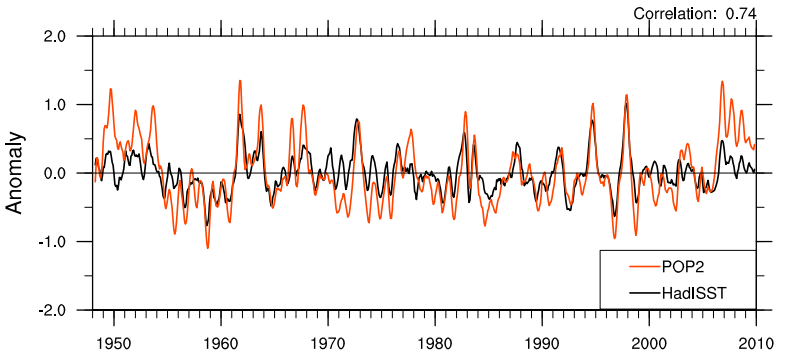

Figure 2. The detrended dipole mode index (DMI) results from the POP2 simulation (red) and the observation data (black) during the period of 1948–2009. The indices were smoothed by calculating the 5 month running mean before being plotted. The correlation coefficient between these two indices is 0.74.

EOF2 also exhibits a dipole pattern, but the anomaly centers are slightly farther north compared with the observations. Bias of the anomaly centers seems to be a common concern in IOD simulations using oceanic models [*Li et al*., 2015].

Figures 1e and 1f show the time series of EOF1 and EOF2 (i.e., PC1 and PC2) for the observations and the model, respectively. A good relation is observed in this figure, with high correlation coefficients of 0.87 and 0.59 between the model and the observations for PC1 and PC2, respectively.

The dipole mode index (DMI) is often used to describe the dipole variability of the SSTAs. It is defined by the difference in the averaged SSTAs between the western (IODW: 50°E–70°E, 10°S–10°N) and eastern (IODE: 90°E–110°E, 10°S–0°) parts of the equatorial Indian Ocean [*Saji et al*., 1999]. Figure 2 compares the DMI values between the observed data and the POP2 results. The modeled DMI is generally consistent with the observed DMI, with a correlation of 0.74 throughout the entire period. This correlation is better than its counterpart reported in *Li et al*. [2002], in which the correlation was calculated to be 0.70 from a 40 year (1958–1997) period using the NCAR ocean model. This improvement may be attributable to the new forcing data (i.e., CORE-II) used in the POP2 run performed in this study. However, the IOD is stronger in the model than in the observation data, as indicated by the amplitudes of the corresponding DMIs, with a standard deviation of 0.47 for the model and 0.34 for the HadISST data during the period of 1948–2009.

One of the main features of the IOD is its broad period. Observations have shown that the IOD has a period of 2–5 years [e.g., *Huang et al*., 2002]. The modeled DMI exhibits a significant period of approximately 3 year (see Figure 7, which will be discussed in detail later), consistent with the observed period of approximately 3.2 year. The maximum power in the POP2 results is approximately 1.5 times that in the HadISST data.

Another well-known feature of the IOD is its so-called phase-locking behavior, i.e., the maximum anomalies usually occur during boreal autumn (September–November). One method to detect the phase-locking of the IOD is to measure the standard deviation of the DMI for each calendar month [*An and Wang*, 2001]. Our calculations show that the maximum standard deviation of the modeled DMI is 0.78 and occurs in September. This is strongly consistent with the observations, in which the DMI peaks in October with a value of 0.44. The larger standard deviation of the modeled DMI indicates that the IOD in the model exhibits stronger variability than that in the observation data, as mentioned previously.

4. Simulation of the IOD in the CESM

4.1. Climatological Fields

In this section, we present the sensitivity experiments conducted using the CESM and evaluate the impacts of the model resolution and atmospheric physics on the IOD. As the first step, we provide an overview of the modeled climatology in these experiments.

Figure 3 shows the difference between the averaged SSTs over 50 year coupled runs and the averaged HadISST data over the period of 1948–2009 for the four experiments: CPL4(2°), CPL4(1°), CPL5(2°), and CPL5(1°) (see Table 1), respectively. As seen in Figure 3, all experiments produce a warm bias over the

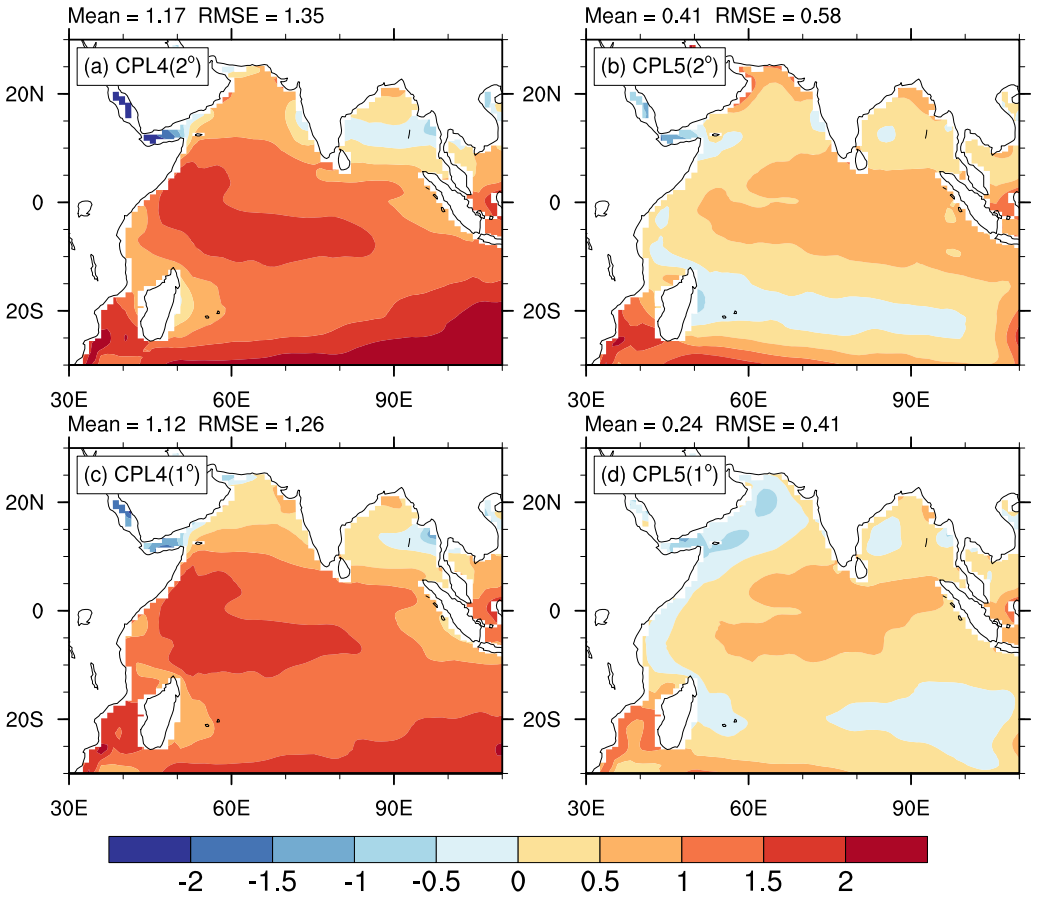

Figure 3. The climatological annual mean biases of the SSTs (°C) with respect to the observations for (a) CPL4(2°), (b) CPL5(2°), (c) CPL4(1°), and (d) CPL5(1°). The regional averaged differences and root-mean-square errors are shown in the top left corner of each plot.

tropical Indian region, especially CPL4(2°) and CPL4(1°). Based on the criteria of the spatially averaged bias and the root-mean-square error (RMSE) over the domain, the performances in the four experiments can be ranked as follows: CPL5(1°) > CPL5(2°) > CPL4(1°) > CPL4(2°). For example, the spatially averaged bias and RMSE over the entire domain are, respectively, 1.17 and 1.35°C for CPL4(2°), and 0.24 and 0.41°C for CPL5(1°). Thus, the physics in CAM5 and the higher resolution of the atmospheric model are beneficial for simulating the tropical Indian SST, particularly the former, which has a greater influence on the SST simulation than does the latter.

The simulation skill can be comprehensively measured using a Taylor diagram [*Taylor*, 2001], which simultaneously presents a visual summary of the centered RMSE, pattern correlation and standard deviation (see the Appendix A for details). Prior to calculating these statistics, the simulated SST is normalized with respect to the corresponding standard deviation of the observation data, such that the reference data set (i.e., observational data) is plotted at polar coordinates (1.0, 0.0). In the Taylor diagram of the four CESM experiments (Figure 4), the ratio of the standard deviation between the simulation and the observation is given by the radial distance from the zero point, as indicated by the dashed circles. Thus, the distance from the dashed circle of radius of 1 measures the difference between the model standard deviation and that of the observation data. The angular axis represents the pattern correlation between the model and the observation, as measured by the interceptions at the bold solid circle of the lines connecting the origin point (0,0) and each colored number. The ratio of centered pattern RMSE to the observed standard deviation is represented by the corresponding distance from the reference (REF), as indicated by the solid circles. A shorter distance between a colored number and REF implies a better model performance.

As seen in Figure 4, the majority of the colored numbers correspond to pattern correlations of larger than 0.9, with the exceptions of CPL4(2°) in spring and winter, for which the correlations are noticeably lower. The ratios of

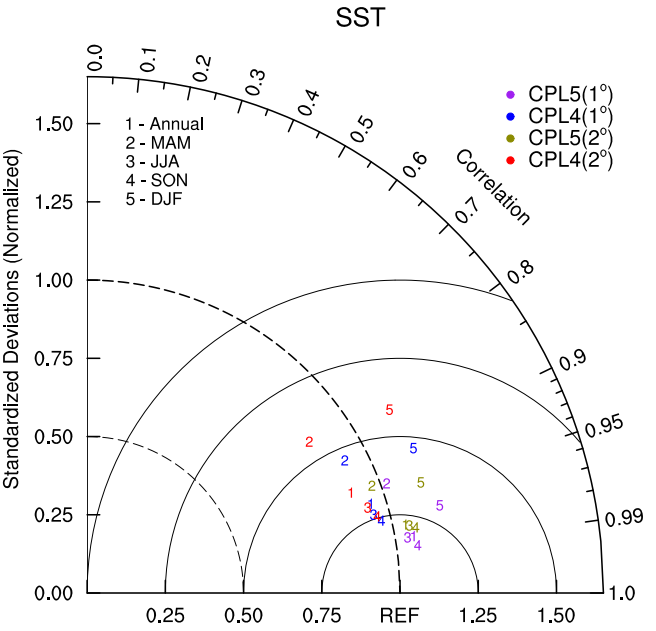

Figure 4. Taylor diagrams for the IOD amplitude, the centered RMSE and spatial correlation between model and observation for the annual and seasonal mean SSTs for the coupled experiments. The reference (REF) represents for the observation data and the model standard deviations are normalized to the scale of the observation data. Numbers 1–5 represent annual, spring (MAM), summer (JJA), autumn (SON), and winter (DJF) values, respectively. Different colors represent the simulations produced in different experiments.

the standard deviation between the simulations and observations range from 0.8 to 1.2 with respect to the dashed circle of radius 1, and the values in winter seem to be the largest. Regarding the centered pattern RMSEs, those for CPL5(1°) are the best, followed by CPL5(2°), CPL4(1°), and CPL4(2°). In general, Figure 4 shows that CPL5(1°) appears superior to the other experiments, especially in autumn, for which the correlation is larger than 0.99 and the ratio of the spatial standard deviation is 1.05. Those findings again indicate that the CAM5 physics and the higher atmospheric resolution are beneficial for the simulation of tropical Indian SSTs. In terms of seasonality, all experiments perform the best in autumn and the worst in winter, probably because of the seasonal variation of the tropical Indian interannual variability, which is strongest in autumn and weakest in winter.

4.2. Interannual Variability of the Tropical Indian Ocean

In this section, we evaluate the simulation skill exhibited in these experiments for the extraction of the interannual variability of the tropical Indian Ocean and particularly for the simulation of the IOD.

Figures 5 and 6 show the first two EOF modes of the SSTAs in the four CESM experiments, and their corresponding PCs. As seen in Figure 5, the results of the coupled experiments using CAM4 (CPL4) exhibit one basin mode and one dipole mode, one each in EOF1 and EOF2. However, the coupled experiments using CAM5 (CPL5) exhibit dipole modes in both EOF1 and EOF2 and lack the basin mode. Figure 6 shows significant interannual variability in both EOF1 and EOF2 for both CPL4 and CPL5. The correlation analysis of these PCs against the DMI confirms the patterns of the EOF modes observed in Figure 5. For example, in CPL5(2°), the correlations of PC1 and PC2 with the DMI are 0.58 and 0.77, respectively. This indicates that EOF2 more closely represents the dipole mode than does EOF1 in CPL5(2°). However, in CPL5(1°), the two leading EOFs both seem to represent the dipole mode well, with correlation coefficients of 0.71 and 0.67, respectively. The spatial correlation between EOF1 in CPL4(2°) and EOF2 in CPL4(1°) is 0.79, and that between EOF2 in CPL4(2°) and EOF1 in CPL4(1°) is 0.94. The spatial correlation of EOF1 between CPL5(2°) and CPL5(1°) is 0.97, whereas the spatial correlation of EOF2 between CPL5(2°) and CPL5(1°) is 0.91. These findings suggest that the atmospheric physics is the dominant factor in determining the EOFs of the SSTAs in these four experiments, whereas the resolutions make only a small difference.

In short, the CPL4 experiments can reproduce one basin mode and one dipole mode in the first two EOF modes, whereas the CPL5 experiments more effectively address the IOD variability. In particular, CPL5(1°) seems incapable of capturing the tropical Indian SSTA basin mode. There are two likely reasons for this finding. First, the CAM5 physics and the higher resolution of the atmospheric model are favorable for capturing the IOD pattern. For example, the spatially consistent variation of the SSTAs is better represented by the basin mode in CPL4 than it is in CPL5, regardless of whether the basin mode is the first or second EOF. By contrast, the dipole pattern is stronger in the 1°-resolution model than in the 2°-resolution model, probably because a model of higher resolution can better capture a spatially skewed structure such as a dipole pattern. This is reflected by the fact that in both CPL4(1°) and CPL5(1°), the first mode is a dipole-like mode, whereas in CPL4(2°) and CPL5(2°), the first mode is the basin mode, as in the observations. Thus, CPL5(1°) seems to yield the strongest IOD structure. Second, the orthogonality of the EOFs may bias the physical interpretation of the second mode of CPL5(1°). It has been found that higher-order modes are often

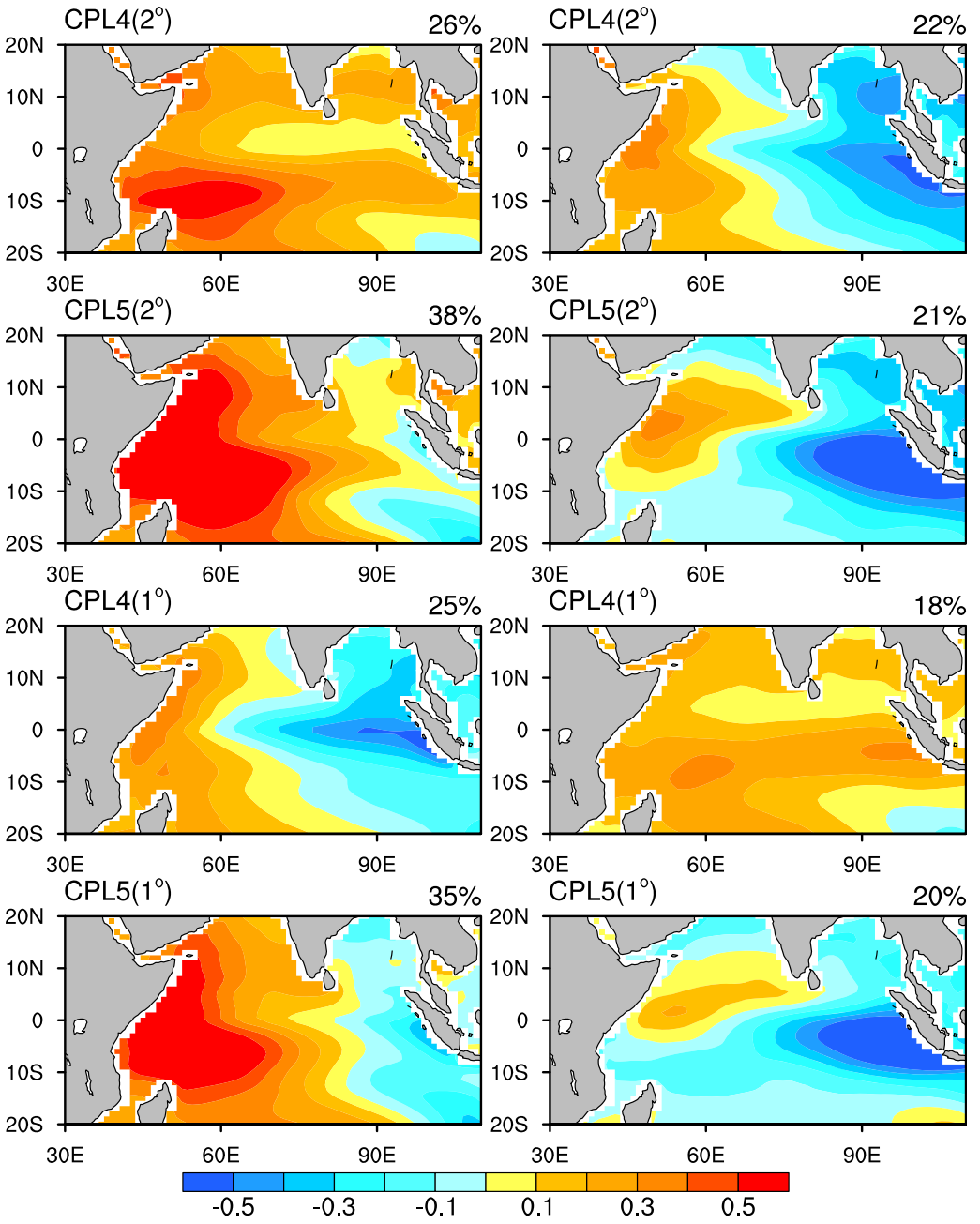

Figure 5. The two leading EOFs of the SSTAs (°C) derived from the four coupled experiments: (first row) CPL4(2°), (second row) CPL5(2°), (third row) CPL4(1°), and (forth row) CPL5(1°). The first and second columns represent EOF1 and EOF2, respectively. The proportions indicated at the top right of each plot represent the variance contributions of each EOF mode.

confined by the orthogonal property of EOFs, and thus, such modes are sometimes called "mathematical modes" [e.g., *Lian and Chen*, 2012]. The impact of orthogonality on EOF2 is expected be very significant in CPL5(1°) since, in this case, EOF1 displays a very strong contrast in patterns of opposite signs between the western and eastern parts of the Indian Ocean.

Figure 7 shows a composite of the wind anomalies and SSTAs for positive IOD events from the observation and simulations. Here the IOD events are defined and chosen in accordance with the criterion that their individual DMI must exceed one standard deviation for five consecutive months; based on this criterion, 9, 12, 9, 10, and 13 IOD events were selected from the observation data and the CPL4(2°), CPL5(2°), CPL4(1°), and CPL5(1°) results, respectively. The composites, which represent a typical life cycle of the IOD as

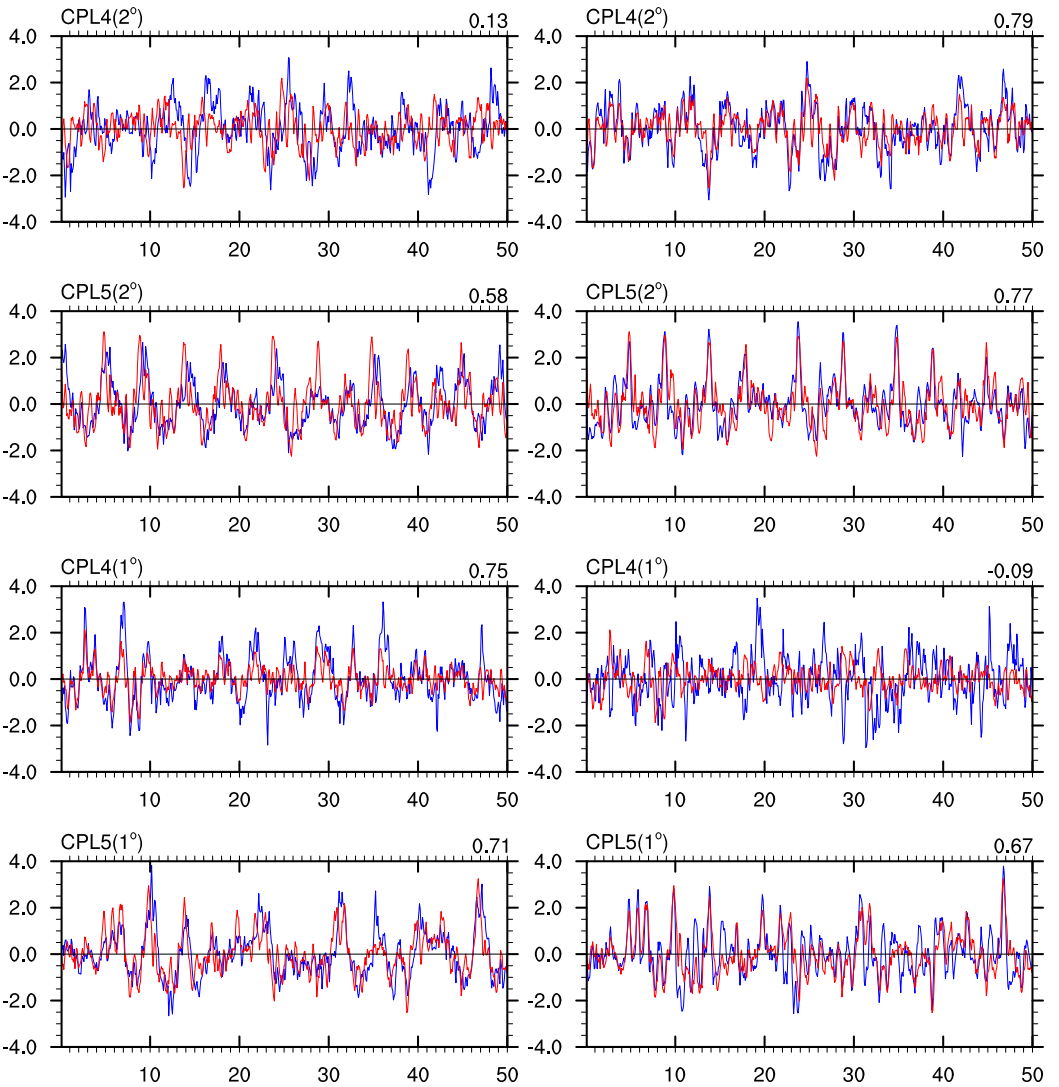

Figure 6. The evolution of the first and second principle components (PC1: left plot, PC2: right plot; blue lines) and the DMI (red lines). The correlations between the individual PCs and the DMI are shown in the top right corner of each plot.

described in *Saji et al.* [1999], span one full year, beginning in March–May (MAM), developing in June–August (JJA), reaching a peak in September–November (SON), and decaying in December–February (DJF).

As seen in Figure 7, each experiment realistically reproduces the IOD life cycle from its onset through its development to its peak. However, the decay phase seems not to be well simulated in any experiment. In the observations, the dipole pattern has disappeared in the DJF period, whereas a visible dipole structure remains in the results of the coupled experiments, particularly for CPL5.

Compared with the observations, all coupled experiments yield stronger amplitudes for both SSTAs and wind anomalies. It is apparent in Figure 7 that the wind anomaly is the strongest in the CPL5(2°) results, followed by CPL5(1°), CPL4(1°), and CPL4(2°). Accordingly, the intensity of the SSTAs shows a similar trend in these experiments, except that the SSTA at the western pole is warmer in CPL4(2°) results than in the CPL4(1°) results, causing the DMI to be larger for CPL4(2°) than for CPL4(1°). Later in the paper, we will further discuss the possible mechanism by which stronger wind anomalies can result in a stronger IOD.

4.3. Period

The period and amplitude of the IOD can be quantified through a power spectrum analysis of the DMI time series, as shown in Figure 8. As seen from this figure, the observation data exhibit a period of approximately

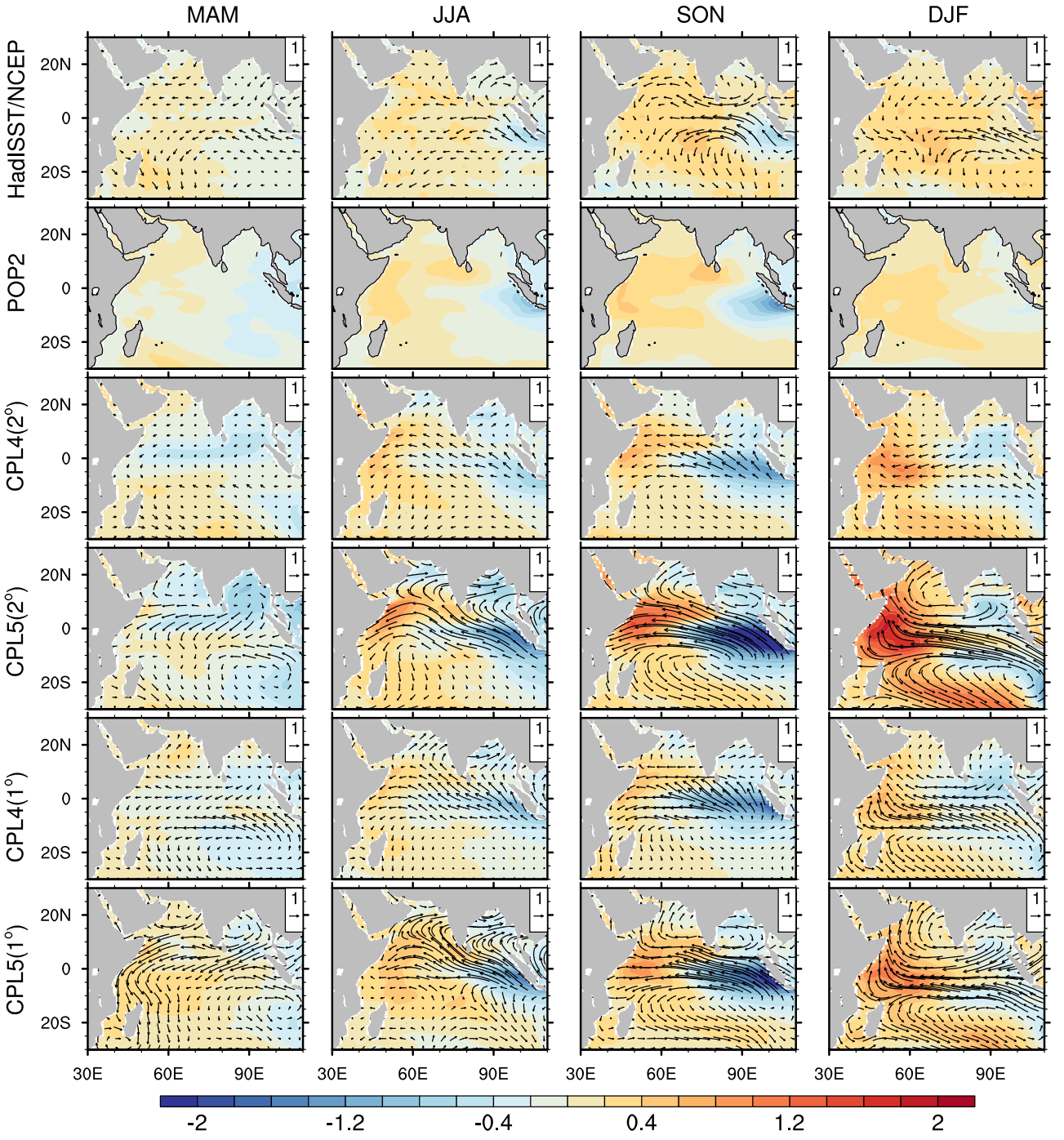

Figure 7. Composite maps of the main evolution of the IOD from observations and experiments for positive events. The first row presents the SST anomalies from the HadISST data and the wind anomalies from the NCEP data. The corresponding SSTA and wind anomaly results from the control run and the coupled experiments are shown in the second through sixth rows.

3.3 year. All of the experimental results capture this period reasonably well, lying with a range of 3–5 years. Aside from the control run, the best simulation of the period is provided by CPL4(1°), followed by CPL5(1°), CPL4(2°), and CPL5(2°).

An interesting feature in Figure 8 is that the period is not strongly dependent on the atmospheric physics, i.e., CPL4 and CPL5 have similar periods when the resolutions are the same. The resolution of the atmospheric model has a much greater influence on the IOD period. This is probably because the higher model resolution can better resolve higher-order waves, resulting in a faster speed of wave propagation

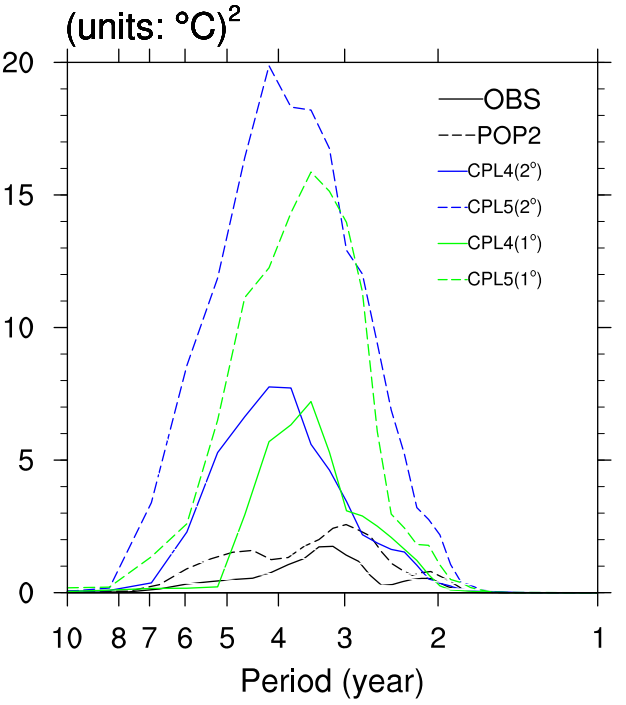

Figure 8. Power spectra of the DMI from the observations and the model experiments: Different colors indicate different cases: observation (solid black), POP2 (dashed black), CPL4(2°) (solid blue), CPL5(2°) (dashed blue), CPL4(1°) (solid green), and CPL5(1°) (dashed green). The band-pass filter with a range of 2–5 year was applied prior to the spectrum analysis.

(e.g., Kelvin or Rossby) and a shorter period. It has been argued that the wave dynamics play an important role in the IOD mechanism, although some details are still unclear [*Gualdi et al*., 2003; *Fischer et al*., 2005].

A comparison of the power spectra shows that the atmospheric physics has a significant influence on the strength of the IOD variability. The CPL5 experiments yield power values twice as high as those of CPL4 for both the 1° and 2° resolution. By contrast, the resolution plays a small role in determining the power. Overall, the effect of the increased model resolution is to shorten the periods and slightly weaken the power. The atmospheric physics has a much greater effect on the power. In section 5, we will analyze possible reasons for the sensitivity results using Bjerknes feedback theory.

4.4. Phase-Locking

An important feature of the IOD is its phase-locking behavior, i.e., its peak always occurs in autumn. Figure 9 shows the standard deviations of the DMI for observations and model experiments. The standard deviations of the models all peak in the fall, with most concentrated in October, as in the observation. The exceptions are POP2 and CPL4(1°), for which the magnitude is slightly larger in September than in October. These results indicate that the models all have a good ability to reproduce the phase-looking, although the amplitudes of the standard deviations are much stronger in the models than in the observations. It should be noted that many other models, including these collected in CMIP5, also have a much stronger IOD than is observed [e.g., *Liu et al*., 2014]. Usually, phase-locking is due to an interaction between the seasonal cycle and the model dynamics. Figure 9 also indicates a good ability of the models to depict the seasonal cycle, which is probably a major reason why the models can produce realistic phase-locking behavior. The other main reason is that the IOD phase-locking is most likely primarily determined by the oceanic model itself, which is the same in all experimental settings.

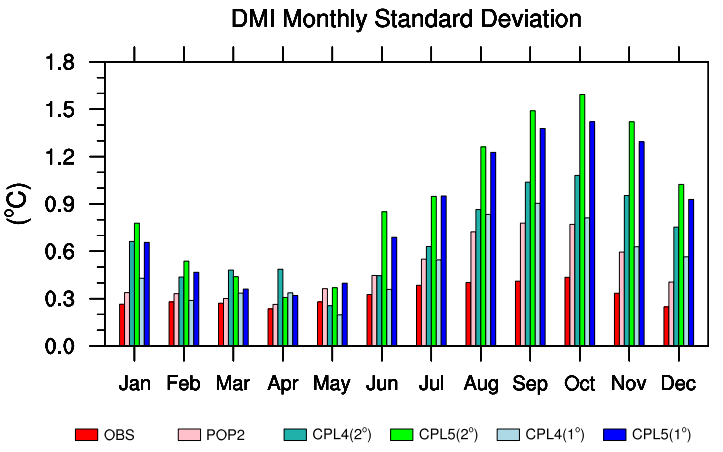

Figure 9. Monthly standard deviation of the DMI for the observations and model experiments, with respect to the calendar month.

5. Bjerknes Feedback Process

A significant bias evident in these experiments lies in their simulation of the IOD strength. As indicated by the composite, power spectrum and standard deviation analyses, the IOD variability is much stronger in the experiments than in the observation, particularly in the CPL5 experiments. Indeed, it is a

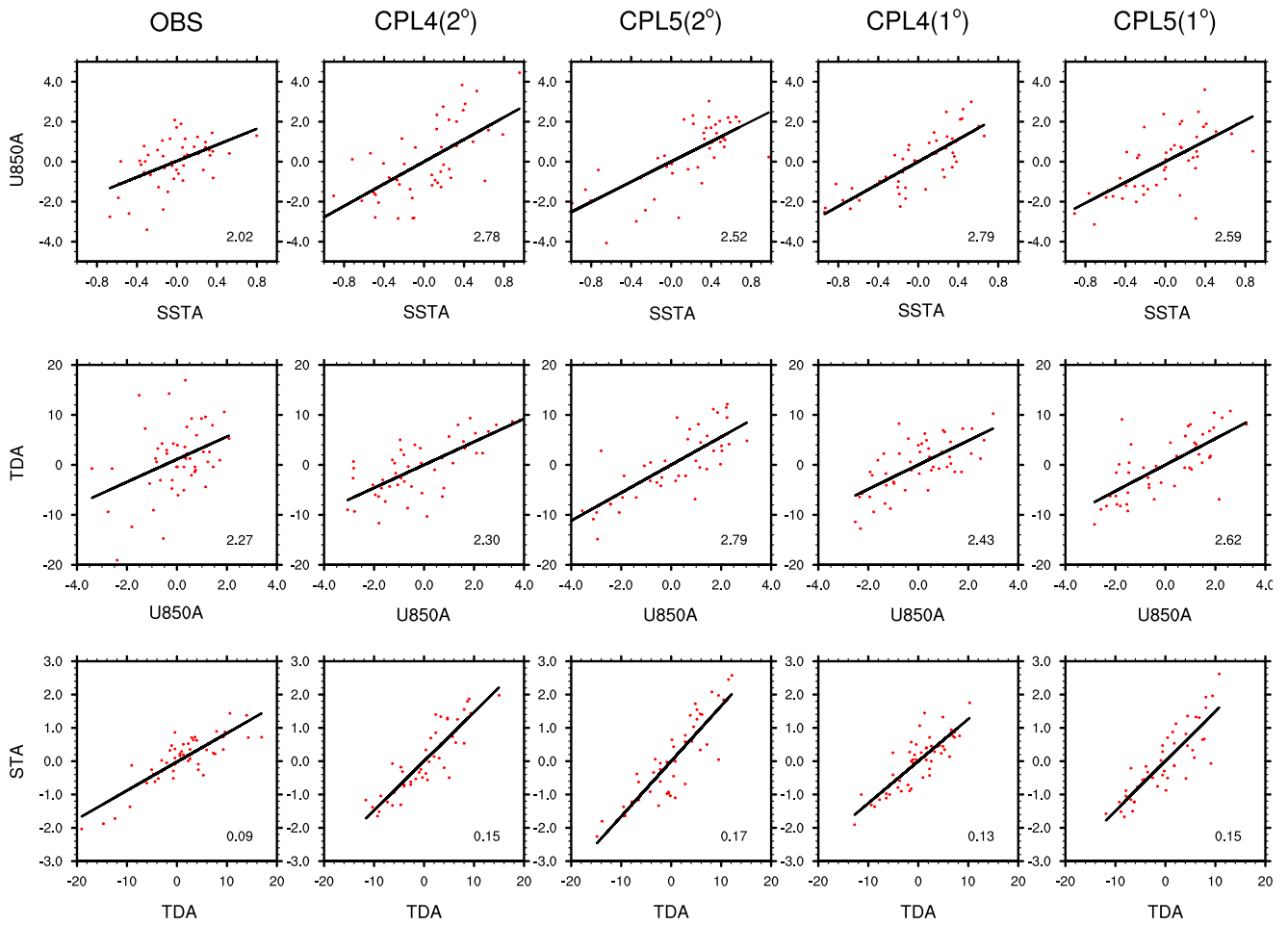

Figure 10. Scatter diagrams revealing the relationships during the IOD development phase (JJA), for both the observations and the coupled experiments, between (top) the 850 hPa zonal wind anomaly (U850A) (m s^{-1}) in the CEIO and the SSTA (K) in the SEIO, (middle) the thermocline depth anomaly (TDA) (m) in the SEIO and the 850 hPa zonal wind anomaly in the CEIO, and (bottom) the subsurface temperature anomaly (STA) (K) and the thermocline depth anomaly in the SEIO. The abscissa represents (top) the SSTA, (middle) the zonal wind anomaly or (bottom) the thermocline depth anomaly. The ordinate represents (top) the zonal wind anomaly, (middle) the thermocline depth anomaly or (bottom) the subsurface temperature anomaly. The slopes of the scatter diagrams are indicated at the bottom right in each plot.

common concern in almost all coupled experiments that the simulated IOD is stronger than the observed IOD [e.g., *Liu et al*., 2011; *Cai and Cowan*, 2013; *Liu et al*., 2014]. It has been convincingly argued that the IOD amplitude is directly linked to the strength of the air-sea feedback process, i.e., the Bjerknes feedback, as reported by *Liu et al*. [2011], *Cai and Cowan* [2013], and *Xie et al*. [2014]. Typically, a stronger Bjerknes positive feedback generates a greater IOD amplitude. The Bjerknes feedback intensity (BFI), defined as shown below, is typicall used to quantitatively measure the Bjerknes feedback process [*Liu et al*., 2011]:

$$BFI = \rho C_w \overline{w} R(u,T) R(D,u) R(T_e,D) \tag{1}$$

where ρ and C_w are the seawater density and specific heat, respectively; $\overline{w}$ denotes the climatological mean vertical velocity at the base of the ocean mixed layer; $R(u,T)$ represents how strongly the 850 hPa zonal wind in the CEIO (5°S–5°N, 70°E–90°E) responds to a unit SSTA forcing in the SEIO (10°S–0°, 90°E–110°E), i.e., SST-wind feedback; $R(D,u)$ represents how the thermocline depth in the SEIO responds to the 850 hPa zonal wind in the CEIO, i.e., wind-thermocline depth feedback; and $R(T_e,D)$ represents how the ocean subsurface temperature (at 70 m) in the SEIO responds to the thermocline depth in the SEIO, i.e., the thermocline depth-subsurface temperature feedback.

From the simplified SST tendency equation, we can calculate each item on the right-hand side of equation (1). Figure 10 shows the SST-wind, wind-thermocline depth, and thermocline depth-subsurface temperature scatter diagrams during the developing phase of the IOD (JJA) for each year. The slopes of the scatter

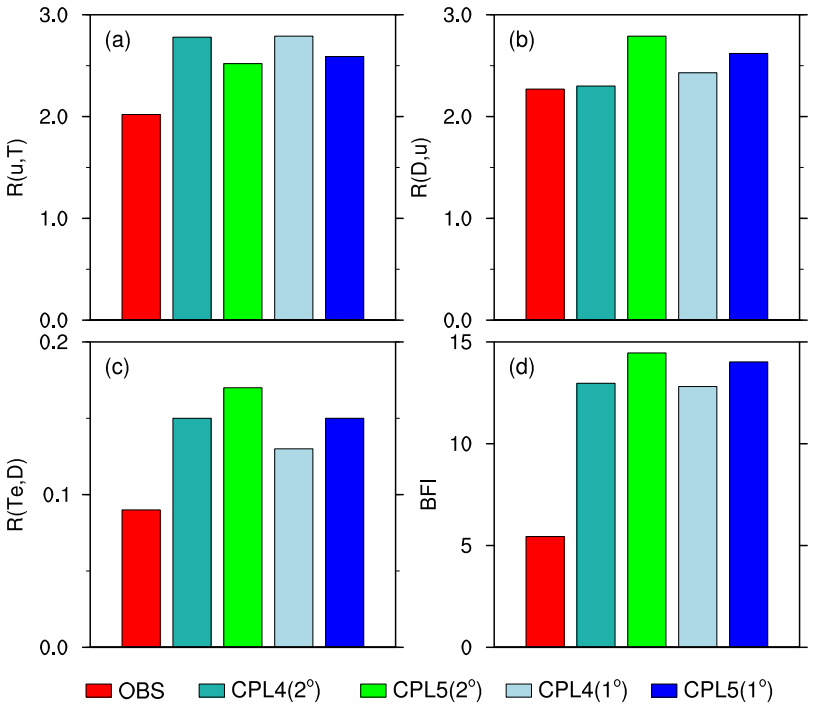

Figure 11. Coupling coefficients (a) $R(u, T)$ (m s^{-1} K^{-1}), (b) $R(D, u)$ (s), (c) $R(T_e, D)$ (K m^{-1}), and (d) BFI (W m^{-2} K^{-1}) during JJA for the observation data and the coupled experiments.

diagrams, as indicated at the bottom right of each plot, are the feedback coefficients, $R(u, T)$, $R(D, u)$, and $R(T_e, D)$, respectively. Compared to the observations, the coupled experiments show similar but steeper slopes upward from left to right. Figure 11d shows the BFI values for the observations and the four coupled experiments. As seen in this figure, the BFI well explains the relationship of the IOD intensity among these experiments, i.e., CPL5(2°) > CPL5(1°) > CPL4(2°) > CPL4(1°) > OBS. This finding is very consistent with the ranking of the IOD amplitudes in these experiments, confirming that the IOD intensity is primarily determined by the air-sea coupling process.

Further investigation enables the diagnosis of the relative contributions of each item on the right-hand side of equation (1) to the BFI. Figures 11a–11c summarize each of these components, illustrating the contribution of the SST-wind feedback, the wind-thermocline depth feedback, and the thermocline depth-subsurface temperature feedback, respectively, to the BFI for the observation data and the four experiments. Figure 11d reveals that the atmospheric physics exerts a stronger effort on the air-sea coupling process than does the resolution, as indicated by the larger BFI value for the CPL5 experiments compared with the CPL4 experiments. In Figure 11a, however, the SST-wind feedback $R(u, T)$ is stronger in CPL4 than in CPL5, which is opposite to the overall results shown in Figure 11d. The mean vertical velocity $\overline{w}$ is also stronger in CPL4 than in CPL5. Thus, the fact that the BFI is stronger in CPL5 than in CPL4 indicates that the wind-thermocline depth feedback $R(D, u)$ and the thermocline depth-subsurface temperature feedback $R(T_e, D)$ are two-dominant factors in determining the BFI. We conclude that the new parameterizations in CAM5, such as the new shallow convective scheme, result in a stronger zonal easterly wind anomaly, and these enhanced easterly winds move the surface water toward the western Indian Ocean, causing the thermocline to deepen in the western Indian Ocean and to become shallower in the eastern Indian Ocean. The shoaling thermocline induces surface and subsurface cooling off the Sumatra-Java coast, which contributes to an anomalous west-minus-east temperature gradient. The cooling surface and subsurface temperatures, in turn, constrain the atmospheric convection along the equatorial Indian Ocean, leading to an anomalous zonal pressure gradient and then consequently strengthening the easterlies zonal wind.

The BFI during the IOD peak (SON) was also examined. It was found that the BFI values are ranked as follows: CPL5(2°) < CPL4(2°) < CPL5(1°) < CPL4(1°) < OBS (not shown). This ranking is nearly opposite to the summer (JJA) ranking discussed above, except for the relationship between CPL4(2°) and CPL5(1°).

This suggests that after the IOD reaches its peak, the stronger feedback process during the development phase should rapidly decay, and the feedback intensity should more quickly decrease during the decay phase. In addition, all BFIs from the experiments are smaller in fall than in summer, indicating that the feedback process is stronger during the IOD development phase than during the IOD peak phase.

6. Indian Summer Monsoon Simulations

In this section, we investigate the simulation of the Indian summer monsoon using the studied coupled models. Figure 12 shows the June–September (JJAS) climatology of the 850 hPa winds over the region of 30°S–30°N and 30°E–120°E of the observation and the model experiments, the JJAS climatology of precipitation of the observation, as well as the model JJAS climatology biases of precipitation. As seen in this figure, heavy rainfall is primarily concentrated over the northern Bay of Bengal, the western Ghat, and the equatorial Indian Ocean region. Comparing the observations with the model simulations reveals that all models exhibit dry biases over the Bay of Bengal and dipole-like east-west biases over the equatorial Indian

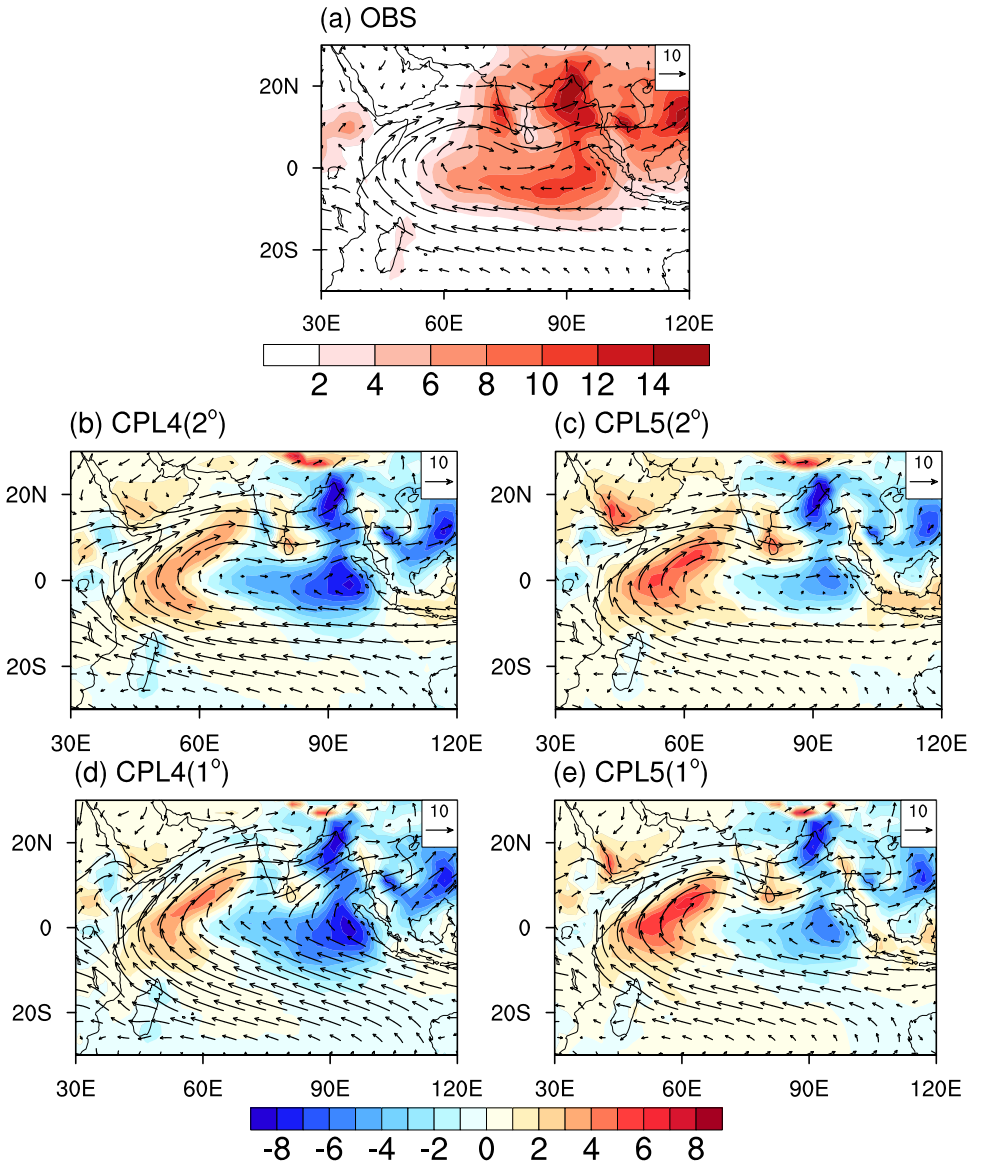

Figure 12. (a) The JJAS climatology of observed precipitation (mm d^{-1}) and 850 hPa winds (m s^{-1}). (b–e) Model JJAS climatology of 850 hPa winds, as well as JJAS climatology biases of precipitation for CPL4(2°), CPL5(2°), CPL4(1°), and CPL5(1°).

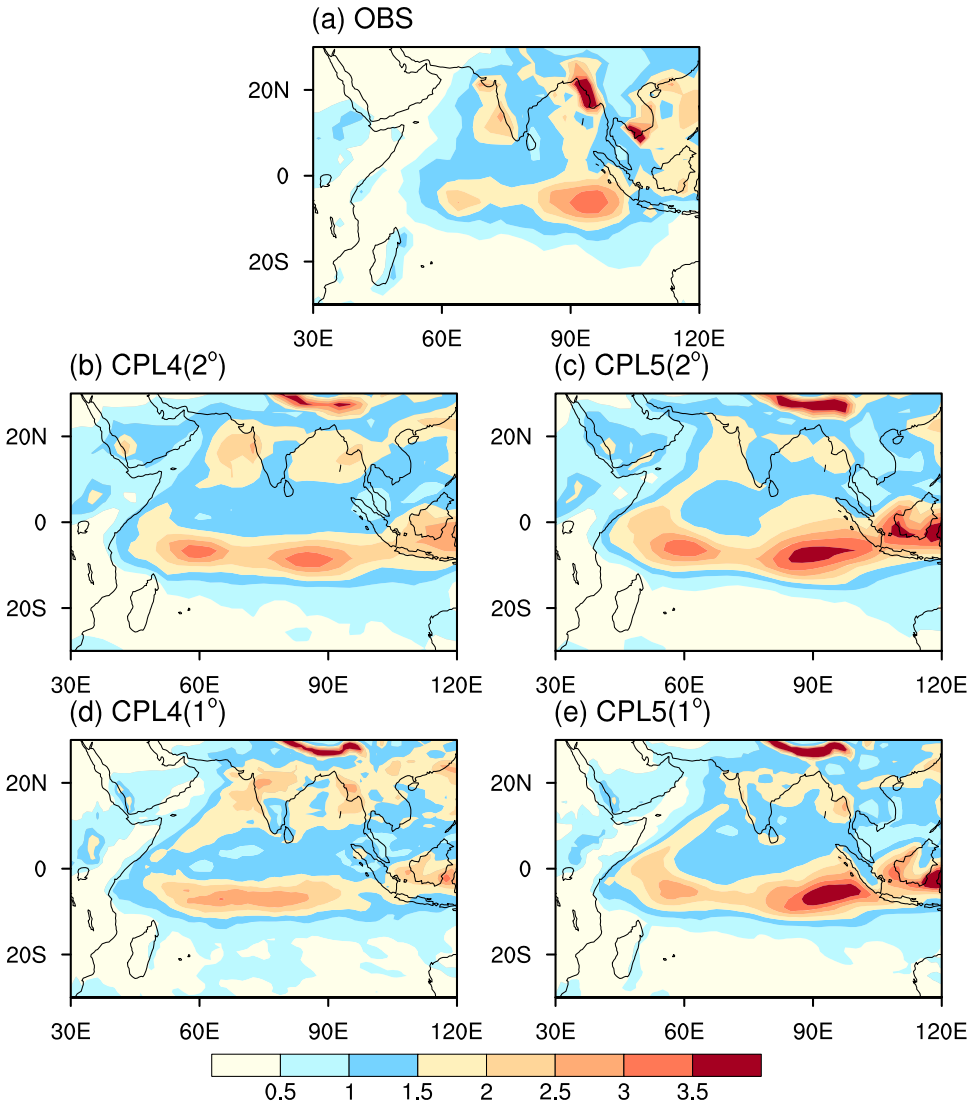

Figure 13. The standard deviations of the JJAS rainfall anomalies (mm d^{-1}) from (a) the observation data (CMAP) and (b–e) the coupled models: (b) CPL4(2°), (c) CPL5(2°), (d) CPL4(1°), and (e) CPL5(1°).

Ocean, with dry biases in the east and wet biases in the west. It seems that the CAM5 physics is beneficial for the simulation of the summer rainfall over the eastern equatorial Indian Ocean, and the CAM4 physics tends to produce less biases over the western equatorial Indian Ocean. However, the atmospheric model resolution has little impact on the rainfall simulation results. It should be noted that the biases over the Indian Ocean also exist in many other models, including those collected in CMIP5 [e.g., *Sabeerali et al.*, 2013].

For winds, the models simulate the cross-equatorial flow over the western Indian Ocean, known as the Findlater Jet [*Findlater*, 1969], reasonably well as compared with the observations. All experiments are well able to simulate the equatorial easterlies, with the exception of CPL4(1°), which produces stronger meridional winds. Evidently, both CPL4(1°) and CPL5(1°) have strong meridional wind biases, indicating that the higher atmospheric model resolution actually degrades the quality of the simulation of the meridional winds over the southern equatorial Indian Ocean.

The standard deviations of the JJAS rainfall anomalies from the coupled models and the observation are shown in Figure 13. Compared with the observations, all coupled models exhibit larger standard deviations, especially in the southern equatorial Indian Ocean and in the western Indian Ocean. The standard deviations of the JJAS rainfall anomalies are larger in the CPL5 experiments than in the CPL4 experiments.

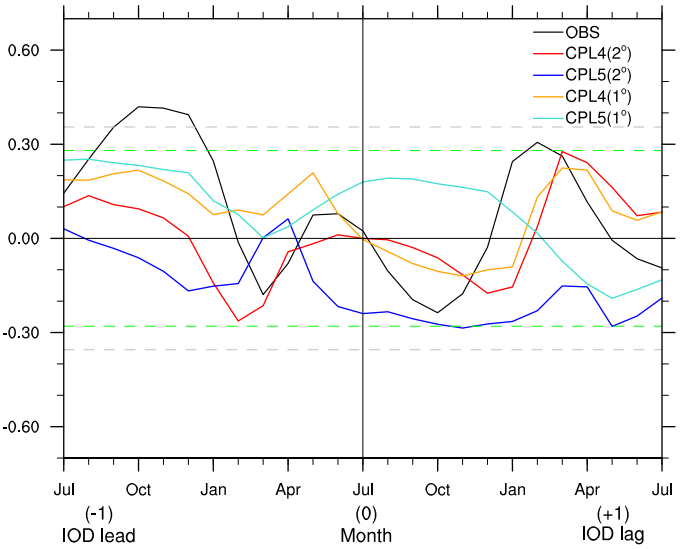

Figure 14. The evolution of lead-lag correlation coefficients between 3 month averaged monthly DMI and JJAS EIMR index in the observation and in the coupled experiments. Here (−1), (0), and (+1) refer to the year before, during, and after the Indian monsoon, respectively. The dashed gray and green lines indicate the 95% significance level for the observation and the coupled experiments, respectively.

The observations found that both the IOD and ENSO have an important influence on the Indian summer monsoon [e.g., *Ashok et al*., 2004; *Cherchi and Navarra*, 2013]. A realistic representation of the IOD-monsoon and ENSO-monsoon relationship is a prerequisite of a successful climate model. For this purpose, we calculated the lagged correlation between the JJAS extended Indian summer monsoon rainfall (EIMR) index and the 3 month averaged monthly DMI for the observation and the studied models, as shown in Figure 14. Here the EIMR index was defined as the mean precipitation anomalies averaged over 5°N–25°N and 60°E–100°E, as defined by *Wu and Kirtman* [2003]. As can be seen, there is a significant positive correlation when the IOD leads monsoon by around 8 months, suggesting a possible impact of IOD on the Indian monsoon rainfall. Such an impact was also reported in *Boschat et al*. [2011], although they used a different index for the Indian monsoon rainfall. Compared to the observation, the IOD-Monsoon relationship is not well captured in models where all correlations are not statistically significant at the confidence level of 95%, although the correlation is higher in the CPL4 experiments than in the CPL5 experiments.

Figure 15 shows the lagged correlation between the JJAS EIMR index and the 3 month averaged monthly Niño-3.4 (170°W–120°W, 5°S–5°N) SSTA index for the observation and the studied models. For the observation, a statistically significant positive correlation at the 95% significance level was found, with the ENSO leading the JJAS monsoon precipitation by 6–9 months; in other words, the preceding fall/winter Niño-3.4 SSTA affects the subsequent JJAS Indian summer rainfall. This result is consistent with the findings of *Wu et al*. [2004], *Shukla and Kinter* [2014], and *Shukla and Huang* [2015]. However, the observed positive correlation is absent in all models. This suggests that the coupled experiments seem unable to correctly capture the impact of ENSO on the Indian monsoon. This is similar to *Shukla et al*. [2014, 2015], which used the NCEP CFSv2 and CFSv1 coupled models, suggesting current challenges in capturing the ENSO-monsoon relation in many coupled models. This is probably due to the fact that different types of ENSO have different impacts on the monsoon, making it difficult for models to capture the ENSO-monsoon relationship [e.g., *Islam and Tang*, 2016].

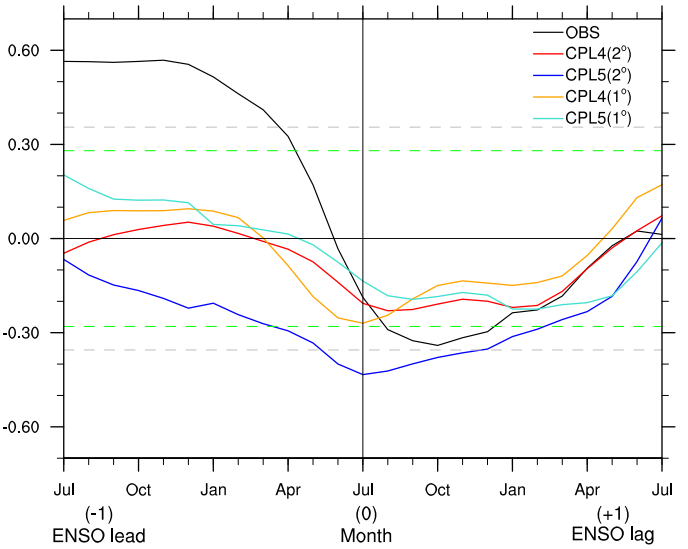

Figure 15. Same as Figure 14, but for the lead-lag correlation coefficients between 3 month averaged monthly Niño-3.4 SST index and JJAS EIMR index.

The relationship between IOD and ENSO has been investigated in numerous studies. For example, it was found that the IOD tends to

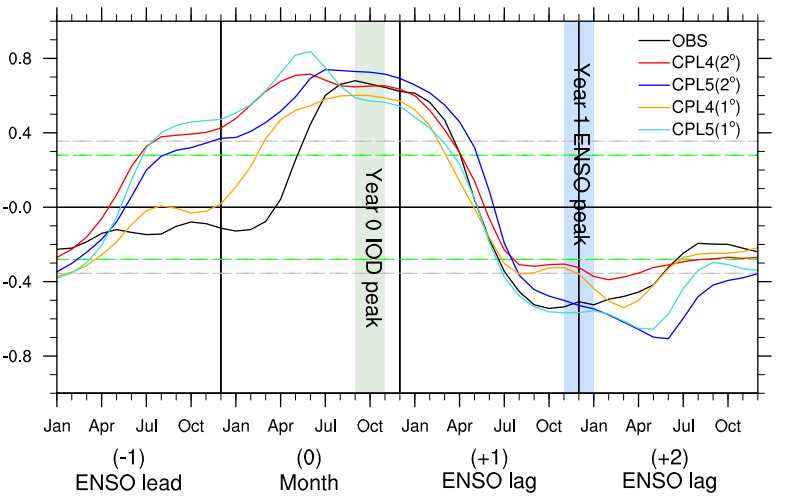

Figure 16. Same as Figure 14, but for the lead-lag correlation coefficients between 3 month averaged monthly Niño-3.4 SST index and SON DMI.

co-occur with ENSO or lead ENSO by 1 year [*Izumo et al.*, 2010]. Figure 16 shows the evolution of lead-lag correlation coefficients between 3 month averaged monthly Niño-3.4 SST index and September–November (SON) DMI. As can be seen, for observation, the maximum positive correlation occurs when ENSO co-occurs with the IOD whereas a maximum negative correlation appears when ENSO lags IOD by around 1 year.

The simultaneous positive correlation of IOD-ENSO supports the opinion that both the IOD and ENSO are different patterns of a tripole mode in the tropical Pacific and Indian Ocean [*Lian et al.*, 2014]. The lagged negative correlation suggests a possible impact of IOD on ENSO. This is probably because a negative IOD event is associated with the warming in the southeast Indian Ocean with a peak at the fall, resulting in a strong convection there. The increased convection in the eastern Indian Ocean strengths the Walker circulation. The easterly wind anomalies accumulate the warm water in the western Pacific, which provides preconditions for ENSO development [*Jin*, 1997]. During a formation of an ENSO positive phase, the easterly wind anomalies start to retreat in the eastern Indian Ocean after November, and collapse in the western and central Pacific soon. This induces warm SST anomalies around the date line in the winter and the spring of the second year. Then, the SST and wind anomalies are further amplified through the Bjerknes feedback, finally inducing the peak phase of ENSO at the fall-winter of second year [*Izumo et al.*, 2010]. The observed IOD-ENSO relationship is well captured in these models, and is better in CPL5 than in CPL4. Figure 16 suggests the possible statistical links of IOD-ENSO. Further study is needed to identify the truth of IOD-ENSO relationship and the underlying mechanism, which is still an open question in this field.

7. Summary and Discussion

In this study, we presented a detailed assessment of the simulation of the IOD using the latest version of the CESM. Emphasis was placed on investigating the impacts of the model resolution and different formulations of the atmospheric physics on simulations of the IOD and the Indian summer monsoon. To this end, two coupled experiments using CAM4 at a high and a low horizontal resolution (CPL4(1°) and CPL4(2°)) were performed. Moreover, because the new version of the CESM includes the updated CAM5 atmospheric physics model, two additional experiments at different resolutions using CAM5 (CPL5(1°) and CPL5(2°)) were also conducted. The main results can be summarized as follows:

1. The CAM5 physics model and the higher atmosphere resolution are beneficial for simulating the tropical Indian SST climatology, with a reduced mean bias and improved pattern correlation with observations.
2. Each experiment could realistically reproduce the IOD life cycle. All experiments effectively simulated the phase-locking of the IOD in the fall. The CAM5 physics seems beneficial for simulating the phase-locking, whereas the atmospheric resolution has little impact on the IOD phase-locking behavior.
3. The IOD period is primarily affected by the atmospheric model resolution, and a higher resolution results in a more realistic period.

4. The IOD intensity in these experiments was predominantly determined by the Bjerknes feedback. The wind-thermocline depth feedback and the thermocline depth-subsurface temperature feedback are two-dominant factors in determining the strength of the IOD.
5. CAM5 results in unrealistically stronger IOD intensity compared with CAM4 when they are coupled with the same ocean model. The model resolution has less impact on the intensity than does the atmospheric physics, but the use of a higher resolution can improve the simulation of the intensity.
6. The CAM5 physics seems beneficial for the simulation of the Indian Ocean JJAS rainfall, whereas a higher atmospheric model resolution tends to result in unrealistically strong meridional winds.
7. The realistic IOD-Monsoon relationship cannot be statistically significantly represented in these experiments although it seems better captured in the CPL4 experiments than in the CPL5 experiments. The significantly positive correlation of ENSO leading the Indian monsoon that appears in observation is absent in all models. The observed IOD-ENSO relationship is well captured in these models, and is better in CPL5 than in CPL4.

As in other coupled models reported in the literature, a notable problem with the IOD simulations performed using these models is an unrealistically strong intensity of the IOD. To investigate this issue, we analyzed the coupling processes in these experiments by diagnosing their Bjerknes feedback indices. It was found that the BFI can well explain the IOD intensity. Further analysis revealed that BFI is primarily dominated by two feedback processes, namely, how strongly the thermocline depth responds to the zonal wind and how strongly the subsurface temperature responds to the thermocline depth. The stronger zonal wind anomaly in CAM5 significantly enhances the two feedback processes.

Studies of the IOD have become a subject of intensive research in the field of tropical air-sea interaction in recent years. This work presents our recent efforts to investigate several possible factors that may impact IOD simulations through sensitivity experiments using the CESM, which serves as a necessary step in improving IOD prediction. The IOD mechanism and the dynamic processes responsible for its basic features are still not completely clear, although there are well-supported hypotheses. Thus, for simplicity and brevity, we have confined our discussions mostly to the analyses and comparisons of the experiments themselves, with some focus on the air-sea coupling feedback process that is primarily responsible for the IOD intensity. Additional sensitivity experiments and comprehensive diagnostic analyses will be needed to understand the dominant physical and dynamical processes of the IOD, particularly regarding such IOD features as the IOD phase conversion and period as well as the relationship among the IOD, the Indian monsoon and the ENSO, which will be pursued in the near future.

Appendix A

A Taylor diagram simultaneously presents the centered root mean square error (RMSE), the pattern correlation and the standard deviation in a visual manner. Given two variables, f_n and r_n, which are sampled at N discrete points, the correlation coefficient R between f and r is defined as:

$$R=\frac{\frac{1}{N}\sum_{n=1}^{N}(f_n-\overline{f})(r_n-\overline{r})}{\sigma_f\sigma_r} \tag{A1}$$

where $\overline{f}$ and $\overline{r}$ are the mean values and σ_f and σ_r are the standard deviations of f (i.e., the model) and r (i.e., the observation), respectively.

The RMSE is defined as:

$$E=\sqrt{\frac{1}{N}\sum_{n=1}^{N}(f_n-r_n)^2} \tag{A2}$$

The difference between the means of the two fields is:

$$A=\overline{f}-\overline{r} \tag{A3}$$

Thus, the centered pattern RMSE is defined as:

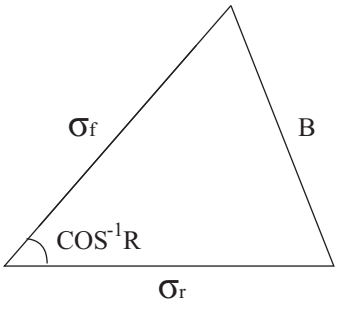

Figure A1. Geometric relationship between the correlation coefficient R, the centered pattern RMSE B, and the standard deviations σ_f and σ_r of the model and reference (observed) fields, respectively.

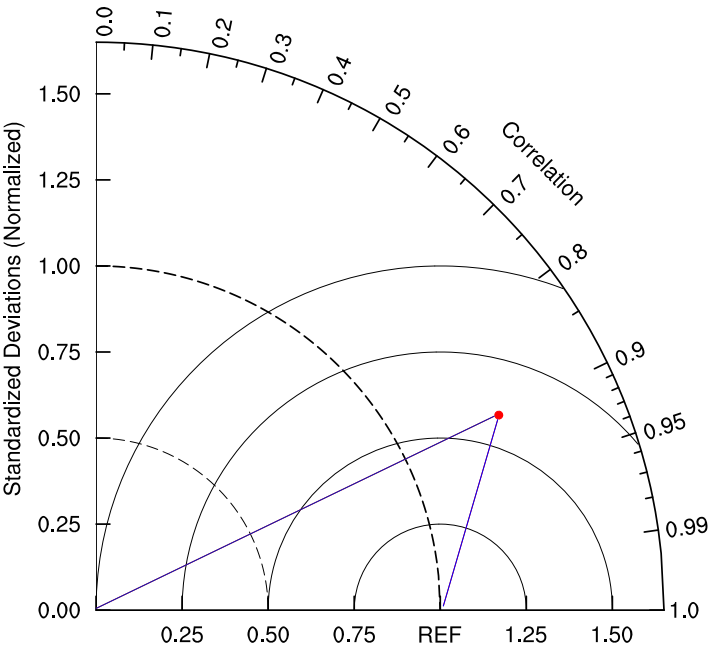

Figure A2. Taylor diagram for displaying pattern statistics after normalization.

$$B=\sqrt{\frac{1}{N}\sum_{n=1}^{N}\left[(f_n-\bar{f})-(r_n-\bar{r})\right]^2} \quad \text{(A4)}$$

The RMSE can be decomposed into two components, A and B [*Taylor*, 2001], as follows:

$$E^2=A^2+B^2 \quad \text{(A5)}$$

All four variables (σ_f, σ_r, R, and B) can be displayed in a single diagram in accordance with the *Law of Cosines*, as shown in Figure A1.

$$B^2=\sigma_f{}^2+\sigma_r{}^2-2\sigma_f\sigma_r R \quad \text{(A6)}$$

Equation (A6) can be normalized by σ_r^2.

$$\frac{B^2}{\sigma_r^2}=\left(\frac{\sigma_f}{\sigma_r}\right)^2+1-2\frac{\sigma_f}{\sigma_r}R \quad \text{(A7)}$$

This equation contains three variables, $\frac{B}{\sigma_r}$, $\frac{\sigma_f}{\sigma_r}$, and R, which form a triangle as shown in Figure A2. The ratio of the standard deviation between the simulation and the observation $\left(\frac{\sigma_f}{\sigma_r}\right)$ is given by the radial distance from the zero point, as indicated by the dashed circles. Thus, the distance from the dashed circle of radius 1 measures the difference between the model standard deviation and that of the observation data. The angular axis (R) represents the pattern correlation between the model and the observation, as measured by the intersection at the bold solid circle of the line connecting the origin point (0,0) and the colored dot. The ratio of the centered pattern RMSE to the observed standard deviation $\left(\frac{B}{\sigma_r}\right)$ is represented by the distance from the reference (REF), as indicated by the solid circles.

Acknowledgments

The observational data sets used in this work can be found at http://apdrc.soest.hawaii.edu/data/data.php. This work was supported by the National Science Foundation of China (41276029, 41530961, and 41321004), National Programme on Global Change and Air-Sea Interaction (GASI-IPOVAI-06, GASI-IPOVAI-04, GASI-IPOVAI-02), State Key Laboratory of Satellite Ocean Environment Dynamics (SOEDZZ1404) and a project of the Second Institute of Oceanography (QNYC201501). YT is also supported by the NSERC (Natural Sciences and Engineering Research Council of Canada) Discovery Grant.

References

An, S.-I., and B. Wang (2001), Mechanisms of locking of the El Niño and La Niña mature phases to boreal winter, *J. Clim.*, *14*, 2164–2176.

Anderson, J., T. Hoar, K. Raeder, H. Liu, and N. Collins (2009), The data assimilation research testbed: A community facility, *Bull. Am. Meteorol. Soc.*, *90*, 1283–1296.

Annamalai, H., R. Murtugudde, J. Potemra, S.-P. Xie, P. Liu, and B. Wang (2003), Coupled dynamics over the Indian Ocean: Spring initiation of the zonal mode, *Deep Sea Res., Part II*, *50*(12), 2305–2330.

Ashok, K., Z. Guan, and T. Yamagata (2003), Influence of the Indian Ocean Dipole on the Australian winter rainfall, *Geophys. Res. Lett.*, *30*(15), 1821, doi:10.1029/2003GL017926.

Ashok, K., Z. Guan, N. H. Saji and T. Yamagata (2004), Individual and combined influences of ENSO and the Indian Ocean Dipole on the Indian Summer Monsoon, *J. Clim.*, *17*(16), 3141–3155.

Baquero-Bernal, A., M. Latif, and S. Legutke (2002), On dipole like variability of sea surface temperature in the tropical Indian Ocean, *J. Clim.*, *15*(11), 1358–1368.

Boschat, G., P. Terray, and S. Masson (2011), Interannual relationships between Indian Summer Monsoon and Indo-Pacific coupled modes of variability during recent decades, *Clim. Dyn.*, *37*(5–6), 1019–1043.

Cai, Q., G. J. Zhang, and T. Zhou (2013), Impacts of shallow convection on MJO simulation: A moist static energy and moisture budget analysis, *J. Clim.*, *26*, 2417–2431.

Cai, W., and T. Cowan (2013), Why is the amplitude of the Indian Ocean Dipole overly large in CMIP3 and CMIP5 climate models?, *Geophys. Res. Lett.*, *40*, 1200–1205, doi:10.1002/grl.50208.

Cai, W., H. H. Hendon, and G. Meyers (2005), Indian Ocean dipole like variability in the CSIRO Mark 3 coupled climate model, *J. Clim.*, *18*(10), 1449–1468.

Carton, J. A., and B. S. Giese (2008), A reanalysis of ocean climate using Simple Ocean Data Assimilation (SODA), *Mon. Weather Rev.*, *136*(8), 2999–3017.

Cherchi, A., and A. Navarra (2013), Influence of ENSO and of the Indian Ocean Dipole on the Indian summer monsoon variability, *Clim. Dyn.*, *41*(1), 81–103.

Collins, W. D., et al. (2006), The community climate system model version 3 (CCSM3), *J. Clim.*, *19*(11), 2122–2143.

Danabasoglu, G. (2008), On multi-decadal variability of the Atlantic meridional overturning circulation in the Community Climate System Model version 3 (CCSM3), *J. Clim.*, *21*, 5524–5544.

Deser, C., M. A. Alexander, S.-P. Xie, and A. S. Phillips (2010), Sea surface temperature variability: Patterns and mechanisms, *Annu. Rev. Mar. Sci.*, *2*, 115–143.

Deser, C., A. S. Phillips, R. A. Tomas, Y. M. Okumura, M. A. Alexander, A. Capotondi, J. D. Scott, Y.-O. Kwon, and M. Ohba (2012), ENSO and Pacific decadal variability in the community climate system model version 4, *J. Clim.*, *25*(8), 2622–2651.
Findlater, J. (1969), A major low-level air current near the Indian Ocean during the northern summer, *Quart. J. R. Meteorol. Soc.*, *95*(404), 362–380.
Fischer, A. S., P. Terray, E. Guilyardi, S. Gualdi, and P. Delecluse (2005), Two independent triggers for the Indian Ocean dipole/zonal mode in a coupled GCM, *J. Clim.*, *18*(17), 3428–3449.
Gent, P. R., S. G. Yeager, R. B. Neale, S. Levis, and D. A. Bailey (2010), Improvements in a half degree atmosphere/land version of the CCSM, *Clim. Dyn.*, *34*(6), 819–833.
Gent, P. R., et al. (2011), The community climate system model version 4, *J. Clim.*, *24*(19), 4973–4991.
Griffies, S. M., et al. (2009), Coordinated ocean-ice reference experiments (COREs), *Ocean Modell.*, *26*(1), 1–46.
Gualdi, S., E. Guilyardi, A. Navarra, S. Masina, and P. Delecluse (2003), The interannual variability in the tropical Indian Ocean as simulated by a CGCM, *Clim. Dyn.*, *20*(6), 567–582.
Huang, B., and J. L. Kinter (2002), Interannual variability in the tropical Indian Ocean, *J. Geophys. Res.*, *107*(C11), 3199, doi:10:1029/2001JC 001278.
Hurrell, J. W., et al. (2013), The community earth system model: A framework for collaborative research, *Bull. Am. Meteorol. Soc.*, *94*(9), 1339–1360.
Iacono, M. J., J. S. Delamere, E. J. Mlawer, M. W. Shephard, S. A. Clough, and W. D. Collins (2008), Radiative forcing by long-lived greenhouse gases: Calculations with the AER radiative transfer models, *J. Geophys. Res.*, *113*, D13103, doi:10.1029/2008JD009944.
Iizuka, S., T. Matsuura, and T. Yamagata (2000), The Indian Ocean SST dipole simulated in a coupled general circulation model, *Geophys. Res. Lett.*, *27*(20), 3369–3372.
Islam, S. U., and Y. Tang (2016), Simulation of different types of ENSO impacts on South Asian Monsoon in CCSM4, *Clim. Dyn.*, doi:10.1007/s00382-016-3117-4.
Islam, S. U., Y. Tang, and P. L. Jackson (2013), Asian monsoon simulations by Community Climate Models CAM4 and CCSM4, *Clim. Dyn.*, *41*(9–10), 2617–2642.
Izumo, T., J. Vialard, M. Lengaigne, C. D. B. Montegut, S. K. Behera, J. J. Luo, S. Cravatte, S. Masson, and T. Yamagata (2010), Influence of the state of the Indian Ocean Dipole on following year's El Niño, *Nat. Geosci.*, *3*(3), 168–172.
Jin, F. F. (1997), An equatorial ocean recharge paradigm for ENSO. Part I: Conceptual model, *J. Atmos. Sci.*, *54*(7), 811–829.
Kalnay, E., M. Kanamitsu, R. Kistler, W. Collins, D. Deaven, L. Gandin, M. Iredell, S. Saha, G. White, and J. Woollen (1996), The NCEP/NCAR 40-year reanalysis project, *Bull. Am. Meteorol. Soc.*, *77*(3), 437–471.
Kay, J. E., B. R. Hillman, S. A. Klein, Y. Zhang, B. Medeiros, R. Pincus, A. Gettelman, B. Eaton, J. Boyle, and R. Marchand (2012), Exposing global cloud biases in the Community Atmosphere Model (CAM) using satellite observations and their corresponding instrument simulators, *J. Clim.*, *25*(15), 5190–5207.
Kirtman, B. P., C. Bitz, F. Bryan, W. Collins, J. Dennis, N. Hearn, J. L. Kinter III, R. Loft, C. Rousset, and L. Siqueira (2012), Impact of ocean model resolution on CCSM climate simulations, *Clim. Dyn.*, *39*(6), 1303–1328.
Klein, S. A., B. J. Soden, and N.-C. Lau (1999), Remote sea surface temperature variations during ENSO: Evidence for a tropical atmospheric bridge, *J. Clim.*, *12*(4), 917–932.
Large, W. G., and S. G. Yeager (2004). Diurnal to decadal global forcing for ocean and sea-ice models: The data sets and flux climatologies, *NCAR Tech. Note NCAR/TN-460+STR*, Natl. Cent. For Atmos. Res., Boulder, Colo., doi:10.5065/D6KK98Q6.
Large, W. G., and S. Yeager (2009), The global climatology of an interannually varying air-sea flux data set, *Clim. Dyn.*, *33*(2–3), 341–364.
Li, G., S. P. Xie, and Y. Du (2015), Monsoon-induced biases of climate models over the tropical Indian Ocean, *J. Clim.*, *28*, 3058–3072.
Li, J., C. Liang, Y. Tang, C. Dong, D. Chen, X. Liu, and W. Jin (2016), A new dipole index of the salinity anomalies of the tropical Indian Ocean, *Sci. Rep.*, *6*, 24260, doi:10.1038/srep24260.
Li, T., Y. Zhang, E. Lu, and D. Wang (2002), Relative role of dynamic and thermodynamic processes in the development of the Indian Ocean dipole: An OGCM diagnosis, *Geophys. Res. Lett.*, *29*(23), 25-21–25-24.
Li, X., Y. Tang, L. Zhou, D. Chen, Z. Yao, and S. U. Islam (2016), Assessment of Madden-Julian oscillation simulations with various configurations of CESM, *Clim. Dyn.*, *47*(7), 2667–2690.
Lian, T., and D. Chen (2012), An evaluation of rotated EOF analysis and its application to tropical Pacific SST variability, *J. Clim.*, *25*(15), 5361–5373.
Lian, T., D. Chen, Y. Tang, and B. Jin (2014), A theoretical investigation of the tropical Indo-Pacific tripole mode, *Sci. China Earth Sci.*, *57*(1), 174–188.
Liu, L., W. Yu, and T. Li (2011), Dynamic and thermodynamic air-sea coupling associated with the Indian Ocean Dipole Diagnosed from 23 WCRP CMIP3 Models, *J. Clim.*, *24*(18), 4941–4958.
Liu, L., S.-P. Xie, X.-T. Zheng, T. Li, Y. Du, G. Huang, and W.-D. Yu (2014), Indian Ocean variability in the CMIP5 multi-model ensemble: The zonal dipole mode, *Clim. Dyn.*, *43*, 1715–1730.
Liu, X., R. Easter, S. Ghan, R. Zaveri, and P. Rasch (2012), Toward a minimal representation of aerosols in climate models: Description and evaluation in the Community Atmosphere Model CAM5, *Geosci. Model Dev.*, *5*, 709–739.
Morrison, H., and A. Gettelman (2008), A new two-moment bulk stratiform cloud microphysics scheme in the Community Atmosphere Model, Version 3 (CAM3). Part I: Description and numerical tests, *J. Clim.*, *21*, 3642–3659.
Neale, R. B., J. H. Richter, and M. Jochum (2008), The impact of convection on ENSO: From a delayed oscillator to a series of events, *J. Clim.*, *21*, 5904–5924.
Neale, R. B., et al. (2010), Description of the NCAR community atmosphere model (CAM 4.0), *NCAR Tech. Note NCAR/TN-485+STR*, 212 pp., Natl. Cent. For Atmos. Res., Boulder, Colo.
Neale, R. B., A. Gettelman, S. Park, A. J. Conley, D. Kinnison, D. Marsh, A. K. Smith and F. Vitt (2012), Description of the NCAR community atmosphere model (CAM 5.0), NCAR Tech. Note NCAR/TN-486+STR, Natl. Cent. For Atmos. Res., Boulder, Colo.
Park, S., and C. S. Bretherton (2009), The University of Washington shallow convection and moist turbulence schemes and their impact on climate simulations with the Community Atmosphere Model, *J. Clim.*, *22*, 3449–3469.
Rayner, N., D. E. Parker, E. Horton, C. Folland, L. Alexander, D. Rowell, E. Kent, and A. Kaplan (2003), Global analyses of sea surface temperature, sea ice, and night marine air temperature since the late nineteenth century, *J. Geophys. Res.*, *108*(D14), 4407, doi:10.1029/2002JD002670.
Renold, M., C. C. Raible, T. F. Stocker, and M. Yoshimori (2010), Simulated resumption of the North Atlantic meridional overturning circulation, *Quat. Sci. Rev.*, *29*, 101–112.

Richter, J. H., and P. J. Rasch (2008), Effects of convective momentum transport on the atmospheric circulation in the community atmosphere model, Version 3, *J. Clim.*, *21*, 1487–1499.
Sabeerali, C. T., D. A. Ramu, D. Ashish, S. Kiran, S. Mahapatra, and S. A. Rao (2013), Simulation of boreal summer intraseasonal oscillations in the latest CMIP5 coupled GCMs, *J. Geophys. Res. Atmos.*, *118*, 4401–4420, doi:10.1002/jgrd.50403.
Saji, N., B. N. Goswami, P. Vinayachandran, and T. Yamagata (1999), A dipole mode in the tropical Indian Ocean, *Nature*, *401*(6751), 360–363.
Shukla, R. P., and J. L. Kinter (2014), Simulations of the Asian monsoon using a regionally coupled-global model, *Clim. Dyn.*, *44*, 827–843.
Shukla, R. P., and B. Huang (2015), Mean state and interannual variability of the Indian summer monsoon simulation by NCEP CFSv2, *Clim. Dyn.*, *42*(2), 1–20.
Sidorenko, D., Q. Wang, S. Danilov, and J. Schröter (2011), FESOM under coordinated ocean-ice reference experiment forcing, *Ocean Dyn.*, *61*(7), 881–890.
Smith, R., P. Jones, B. Briegleb, F. Bryan, G. Danabasoglu, J. Dennis, J. Dukowicz, C. Eden, B. Fox-Kemper, and P. Gent (2010), The parallel ocean program (POP) reference manual: Ocean component of the community climate system model (CCSM), Tech. Note LAUR-10-01853, Los Alamos Natl. Lab., Los Alamos, N. M.
Spencer, H., R. T. Sutton, J. M. Slingo, M. Roberts, and E. Black (2005), Indian Ocean climate and dipole variability in Hadley Centre coupled GCMs, *J. Clim.*, *18*(13), 2286–2307.
Subramanian, A. C., M. Jochum, A. J. Miller, R. Murtarudde, R. B. Neale, and D. E. Waliser (2011), The Madden-Julian Oscillation in CCSM4, *J. Clim.*, *24*, 6261–6282.
Taylor, K. E. (2001), Summarizing multiple aspects of model performance in a single diagram, *J. Geophys. Res.*, *106*(D7), 7183–7192.
Uppala, S. M., P. Kållberg, A. Simmons, U. Andrae, V. D. Bechtold, M. Fiorino, J. Gibson, J. Haseler, A. Hernandez, and G. Kelly (2005), The ERA-40 re-analysis, *Quart. J. R. Meteorol. Soc.*, *131*(612), 2961–3012.
Vavrus, S., and D. Waliser (2008), An improved parameterization for simulating Arctic Cloud Amount in the CCSM3 climate model, *J. Clim.*, *21*, 5673–5687.
Venzke, S., M. Latif, and A. Villwock (2000), The coupled GCM ECHO-2. Part II: Indian ocean response to ENSO, *J. Clim.*, *13*(8), 1371–1383.
Vertenstein, M., A. Bertini, T. Craig, J. Edwards, M. Levy, A. Mai, and J. Schollenberger (2013), *CESM User's Guide (CESM1.2 Release Series User's Guide)*, NCAR. [Available at http://www.cesm.ucar.edu/models/cesm1.2/cesm/doc/usersguide/ug.pdf.]
Vinayachandran, P., S. Iizuka, and T. Yamagata (2002), Indian Ocean dipole mode events in an ocean general circulation model, *Deep Sea Res., Part II*, *49*(7), 1573–1596.
Vinayachandran, P., P. Francis, and S. Rao (2009), Indian Ocean dipole: Processes and impacts, *Curr. Trends Sci.*, Indian Academy of Sciences, India, pp. 569–589.
Webster, P. J., A. M. Moore, J. P. Loschnigg, and R. R. Leben (1999), Coupled ocean-atmosphere dynamics in the Indian Ocean during 1997–98, *Nature*, *401*(6751), 356–360.
Wu, R., and B. P. Kirtman (2004), Impacts of the Indian Ocean on the Indian Summer Monsoon ENSO relationship, *J. Clim.*, *17*(15), 3037–3054.
Xie, P., and P. A. Arkin (1997), Global precipitation: A 17 year monthly analysis based on gauge observations, satellite estimates, and numerical model outputs, *Bull. Am. Meteorol. Soc.*, *78*, 2539–2558.
Yu, J.-Y., and K. Lau (2005), Contrasting Indian Ocean SST variability with and without ENSO influence: A coupled atmosphere-ocean GCM study, *Meteorol. Atmos. Phys.*, *90*(3–4), 179–191.